Test of charged baryon interaction with high-resolution vibrational spectroscopy of molecular hydrogen ions

S. Alighanbari ⬤ , I. V. Kortunov, G. S. Giri ⬤ & S. Schiller ⬤ ✉

Molecular hydrogen ions are of high interest in fundamental physics and metrology. In particular, the long-range baryon–baryon interaction and the degrees of freedom of baryon rotational and vibrational motion are key features of molecular hydrogen ions. Here we present the measurement of a one-photon transition of HD⁺, a fourth overtone vibrational transition. Through a comparison of experimental and ab initio frequencies of this and previously measured transitions, we implement a test of the low-energy quantum physics of baryon interaction and motion. The results may also be interpreted as a test of Weinberg's quantum mechanics extension. Furthermore, we compare the value of the fundamental constant combination $\mu/m_e = m_p m_d/(m_p + m_d)m_e$ determined from our measurement with the value obtained from mass spectrometry experiments. This may also be regarded as a test of the quantum behaviour of baryons, revealing a moderate tension of 1.7 times the combined uncertainty. Combining our measurement result with some previous ones on HD⁺, we obtain a least-squares-adjusted value for μ/m_e as well as a bound for the force between the proton and deuteron in a scenario that is beyond the Standard Model of particle physics. No evidence of a deviation from conventional quantum physics is found.

Because of their relative simplicity, molecular hydrogen ions (MHI) are calculable molecules. Applying the theory of non-relativistic quantum electrodynamics (NRQED)[1], Korobov and Karr[2] calculated vibrational transition frequencies with fractional uncertainty estimated to be 8×10^{-12}, limited by uncalculated NRQED contributions of high order in the fine structure constant α. This uncertainty is within a factor of 10 of the theory uncertainty achieved for the hydrogen atom. NRQED theory assumes, in particular, the conventional Coulomb interaction between the two baryons in the MHI. Actual predictions of MHI frequencies require the values of certain fundamental constants as the input, specifically the Rydberg constant R_∞, the ratio of the masses of the specific baryons (proton, deuteron, triton) relative to the electron mass and the charge radii of those baryons. Given that the predictions of the ab initio theory are so accurate, if the spectroscopy of MHI matches or surpasses this accuracy, it becomes possible to either accurately determine the mentioned fundamental constants or test for the presence of unconventional, hypothetical interactions, assuming values of constants measured on other systems. Recently, this has been implemented on a rotational transition and two vibrational transitions[3–5] that were measured with sub-Doppler resolution. We extend that work concerning three main aspects. First, we extend a spectroscopic technique—trapped ion cluster transverse excitation spectroscopy—to a shorter wavelength and substantially higher resolution. Second, we consequently achieve a metrological study of a previously unexplored transition—the fourth overtone vibrational transition of HD⁺—with experimental accuracy higher than the theory prediction. Third, our data, by themselves or combined with previous data, enable two tests of quantum physics—one that relates to the Weinberg's

Institut für Experimentalphysik, Heinrich-Heine-Universität Düsseldorf, Düsseldorf, Germany. ✉e-mail: step.schiller@hhu.de
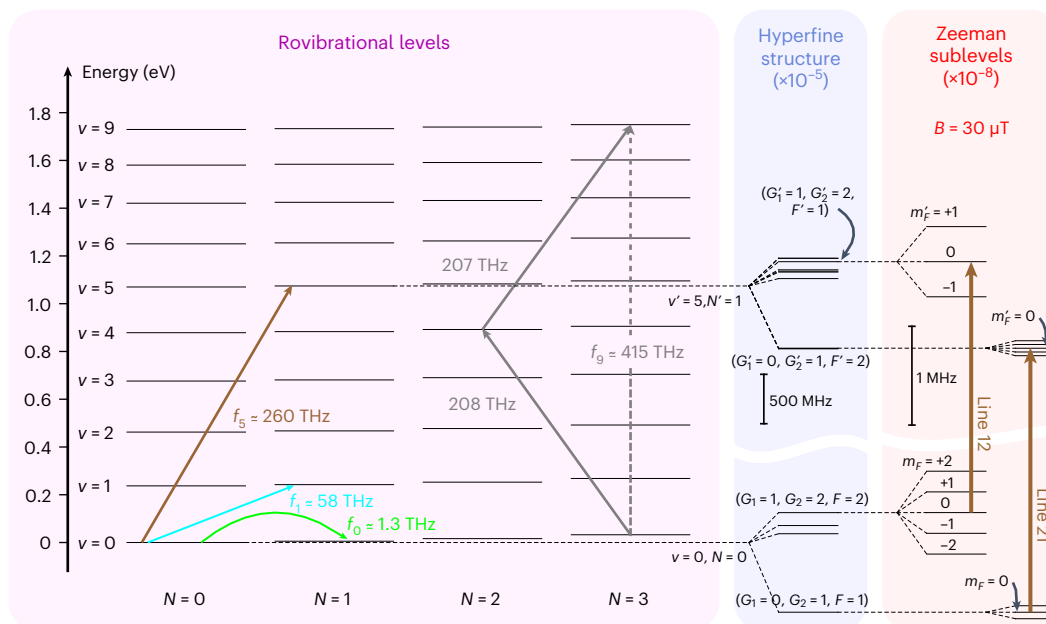
Fig. 1 | Selected states of HD⁺ and transitions relevant to this work. A subset of the rovibrational energy levels (left). The brown arrow shows the one-photon transition f_5, namely, $(v = 0, N = 0) \rightarrow (v' = 5, N' = 1)$, measured in this work. The other coloured arrows indicate transitions previously measured with high accuracy: f_0 (ref. [3]), f_1 (ref. [4]) and f_9 (a two-photon transition)[34]. Hyperfine structures of the two rovibrational levels $(v = 0, N = 0)$ and $(v' = 5, N' = 1)$ (middle). Here F is the total angular momentum of the molecule, G_1 is the total spin of the proton–electron pair and G_2 is the total particle spin, also including the deuteron. The two particular Zeeman components measured in this work, line 12 and line 21, are also shown (right, in brown). Here B is the nominal applied magnetic field, and m_F is the projection quantum number. The horizontal dashed lines connect equal states in each panel, and the differing energies of the three panels are indicated. Extended Data Fig. 4 provides the details.

analysis of Lindblad quantum mechanics[6] and the other, more generic. Likewise, the comparison of our present determination of the baryon–electron mass ratio μ/m_e with the Penning-trap-based determination is interpreted as a test of baryonic quantum mechanics. Here μ is the reduced nuclear mass, $\mu^{-1} = m_p^{-1} + m_d^{-1}$, and m_e is the electron mass. Finally, we contribute in improving the bounds to a hypothetical beyond-Standard-Model (BSM) force between the baryons.

The achieved accuracy for a one-photon transition also has important implications for future work: it will be possible to perform spectroscopy of similar accuracy on a large set of transitions in the MHI, thus enabling a wide-ranging exploration of their energy spectrum.

The transition we studied, namely, $(v = 0, N = 0) \rightarrow (v' = 5, N' = 1)$ (v and N are the vibrational and rotational quantum numbers, respectively) is depicted in the energy diagram (Fig. 1) as brown arrows. Its frequency, $f_5 \simeq 260$ THz, lies between the previously studied one-photon fundamental transition ($f_1 \simeq 58$ THz (ref. [4])) and the two-photon high-overtone transition ($f_9 \simeq 415$ THz (ref. [5])).

We perform resonance-enhanced multiphoton photodissociation (REMPD) spectroscopy on an ensemble of HD⁺ ions trapped in a linear radiofrequency (RF) trap, using infrared photons (1.15 μm) to excite a vibrational transition and ultraviolet photons (266 nm) to dissociate the molecule. The molecules are sympathetically cooled by laser-cooled beryllium ions[7]. The smaller mass of HD⁺ compared with Be⁺ leads to a spatial segregation of the lighter ions that arrange in the vicinity of the trap axis. If a small number of lighter ions is loaded, they arrange in a string-like fashion along the trap axis[8]. For ions in a string, the amplitude of residual thermal (secular) motion along the perpendicular direction becomes comparable with the wavelength of infrared radiation, provided the sympathetic cooling is sufficiently strong. When a mid-infrared spectroscopy wave is directed perpendicular to the trap axis (trapped ion cluster transverse excitation spectroscopy), an ultranarrow carrier can be observed in the excitation spectrum[4]. Here we show that this is also the case for a comparatively short spectroscopy wavelength of $\lambda = 1.15$ μm. Importantly, we achieve

a fractional uncertainty of the individual systematic shifts comparable with the previous study. This is, in part, enabled by the use of an ultranarrow-linewidth spectroscopy laser having excellent long-term frequency stability (see 'Apparatus' section and Extended Data Fig. 1).

We focus on the two hyperfine components, namely, line 12 and line 21 (Fig. 1). For each line, we report the Zeeman component $m_F = 0 \rightarrow m_F' = 0$. Here m_F and m_F' are the projections of the total angular momenta F and F' on the static magnetic-field direction. These particular Zeeman components are chosen for their small quadratic Zeeman shifts (see 'Systematic shifts' section). Figure 2 shows the Zeeman components observed under different operating conditions. Power broadening of the transition by the spectroscopy laser wave is kept moderate by using a sufficiently low power (Fig. 2a(i)(ii)). The narrowest observed line (Fig. 2(ii), dashed red) had a full-width at half-maximum below 0.4 kHz, corresponding to a line resolution of 6×10^{11}. To the best of our knowledge, this is the highest resolution ever observed on any molecular ion (another work[4] provides a brief review), and even surpasses the best resolution of rotational spectroscopy[3]. Our present resolution is nearly the same as the best resolution achieved on ultracold neutral molecules[9]. The linewidths are due to a combination of power broadening, short exposure, spectroscopy laser linewidth and frequency instability. The transitions have a theoretical natural linewidth of approximately 10 Hz (ref. [10]).

Table 1 summarizes the results of the systematic shifts. We find that shifts induced by external fields are barely detectable given our transition linewidths. The only important correction is the recoil shift. The unperturbed frequencies are

$$f_{\text{line12}}^{(\text{exp})} = 259,762,914,375.3(0.9)_{\text{exp}} \text{ kHz} ,$$
$$f_{\text{line21}}^{(\text{exp})} = 259,763,040,467.8(0.8)_{\text{exp}} \text{ kHz} . \tag{1}$$

The ab initio theory of the MHI's hyperfine structure[11–13] furnishes the spin frequencies $f_{\text{spin},12}^{(\text{theor})}$ and $f_{\text{spin},21}^{(\text{theor})}$, together with an estimate of
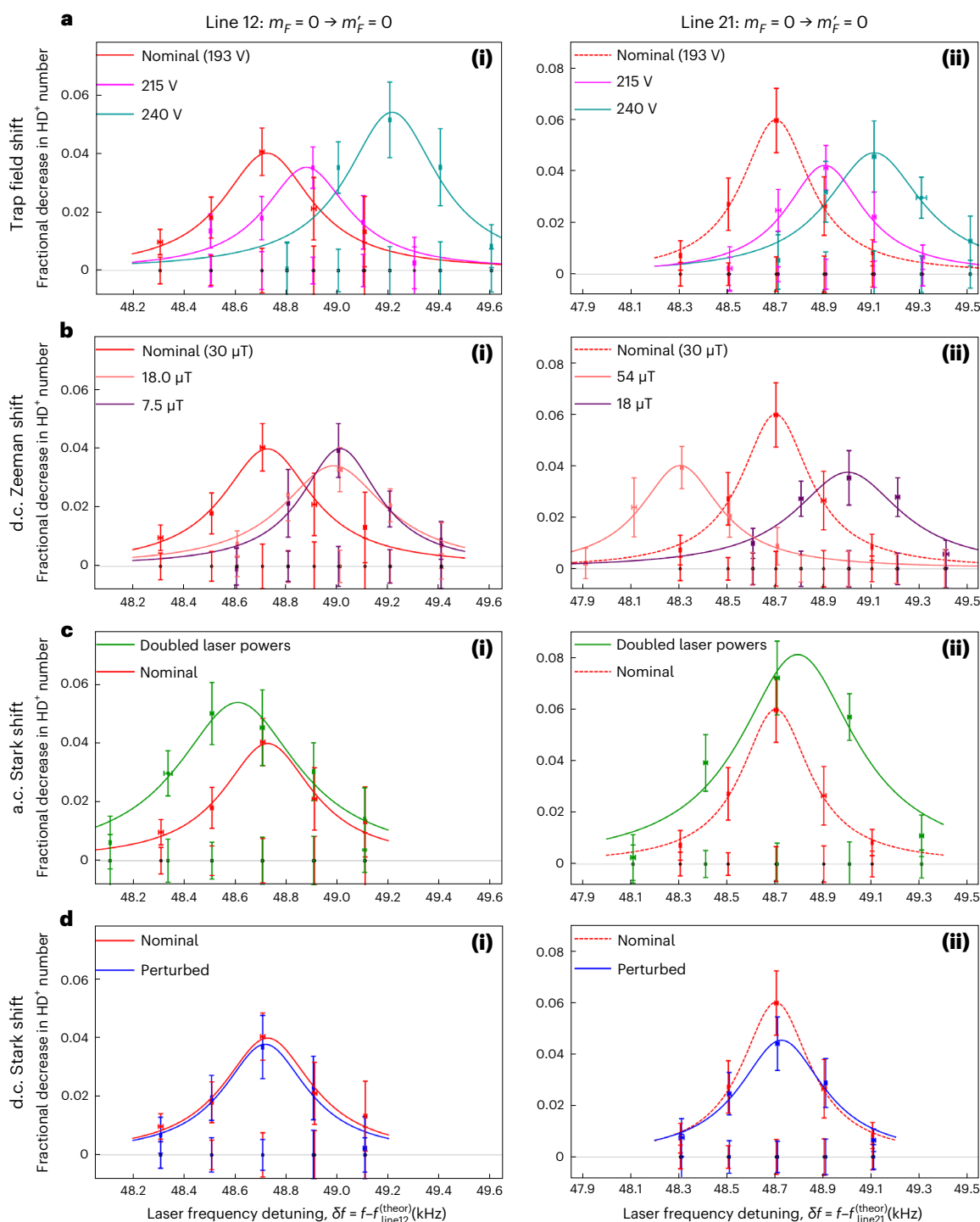
Fig. 2 | Two hyperfine components at $f_5 \simeq 260$ THz, measured under different operating conditions. a–d, Zeeman component $m_F = 0 \rightarrow m_F' = 0$ of line 12 (left). The same data for line 21 (right). The rows from top to bottom show the lines measured to determine the systematic shifts caused by the trap RF field (**a**(i) and **a**(ii)), d.c. Zeeman (**b**(i) and **b**(ii)), a.c. Stark (**c**(i) and **c**(ii)) and d.c. Stark (**d**(i) and **d**(ii)) effects. The red full and dashed lines and the corresponding data points are line 12 and line 21, respectively, measured under nominal operating conditions. These two lines are reproduced in all the panels in each column.

Other colours: line 12 and line 21 taken after changing an external parameter. 'Systematic shifts' section provides details of the systematic shift measurements. For display purposes, the data are divided into 200-Hz- or 300-Hz-wide bins. The horizontal error bars represent the standard deviation of the frequency values in the bin. The vertical error bars represent the standard error of the mean of the data in the frequency bin. The full and dashed lines are Lorentzian fits to the data points. The data points (framed in black) are the mean background decay. They were obtained with the spectroscopy wave off.

their uncertainties (see 'Ab initio theory of transition frequency' section and Extended Data Table 1). Subtracting them from the experimental frequencies $f_{\text{line12}}^{(\text{exp})}$ and $f_{\text{line21}}^{(\text{exp})}$ and forming an optimized linear combination (see 'Composite frequency' section), we obtain the spin-averaged experimental transition frequency as

$$f_5^{(\text{exp})} = f_{\text{spin-avg}}^{(\text{exp})} = 259, 762, 971, 051.2(0.6)_{\text{exp}}(0.04)_{\text{theor,spin}} \text{ kHz}. \tag{2}$$

The total fractional uncertainty is 2.3×10^{-12}. For simplicity, we have assigned the (negligible) theoretical uncertainty associated with

Table 1 | Error budget

Effect	$f_{\text{line12}}^{(\text{exp})} - f_{\text{line12}}^{(\text{exp,nom})}$	$f_{\text{line21}}^{(\text{exp})} - f_{\text{line21}}^{(\text{exp,nom})}$
Statistics	0.00(21)	0.00(17)
Trap field	−0.86(70)	−0.71(68)
d.c. Zeeman	0.33(19)	0.27(21)
a.c. Stark	−0.12(35)	0.07(38)
d.c. Stark	0.00(21)	0.00(17)
Maser offset	1.76	1.76
Recoil	−49.58	−49.58
Total	−48.46(86)	−48.18(84)

Measured systematic shifts and their uncertainties, and the statistical uncertainty of two spin components at 260 THz. All the values are given in kHz. Here $f_{\text{line } i}^{(\text{exp})}$ is the extrapolated, unperturbed frequency value and $f_{\text{line } i}^{(\text{exp,nom})}$ is the frequency value under standard operating conditions.

the predicted spin frequencies (0.035 kHz) to the experimental value.

Ab initio theory[2] also provides the prediction of the spin-averaged frequency (Extended Data Table 2), which depends on the assumed values of R_∞, nuclear charge radii r_p and r_d, and mass ratios m_p/m_e and m_d/m_e. For the first three quantities, we use the values currently recommended by the Committee on Data of the International Science Council (CODATA)[14] and take into account the fact that the mass ratio dependency is predominantly in terms of the normalized reduced nuclear mass μ/m_e. Then, we can determine the ratio μ/m_e from the theoretical and experimental spin-averaged frequencies by solving the equation $f_{\text{spin-avg}}^{(\text{theor})}(\mu/m_e) = f_{\text{spin-avg}}^{(\text{exp})}$ (see 'Ab initio theory of transition frequency' section). We obtain

$$\mu/m_e = 1,223.899228720(7)_{\text{exp}}(24)_{\text{theor,QED}}(0)_{\text{theor,spin}}(3)_{\text{CODATA2018}}. \tag{3}$$

The last uncertainty contribution originates from the nuclear charge radii and R_∞. The fine structure constant enters the frequency values only at fractional order α^2 (Extended Data Table 2); therefore, its current uncertainty is negligible in the present context. The total fractional uncertainty is $u_r(\mu/m_e) = 2.0 \times 10^{-11}$.

Now, four independent accurate experimental transition frequencies of HD$^+$ are available: three vibrational (f_1 (ref. [4]), f_5 (this work) and f_9 (ref. [5])) and one rotational (f_0 (ref. [3])). Extended Data Table 3 summarizes their key results. In view of current inconsistencies[15], here we mainly focus on the pair f_1 and f_5. For the purpose of testing quantum theory, we consider two analyses (I and II) based on simple combinations of two transition frequencies, one analysis (III) based on a comparison with Penning trap measurements and finally (analysis IV), we discuss setting a bound to the strength of a BSM proton–deuteron force.

(I) Certain contributions to the uncertainties of the individual $f_{\text{spin-avg}}^{(\text{theor})}$ are currently considerably larger than the uncertainty of $f_{\text{spin-avg}}^{(\text{exp})}$ (Extended Data Table 3). Combinations of theoretical frequencies substantially reduce the influence of various QED contributions and of constants' uncertainties (see 'Frequency combinations with reduced sensitivity to fundamental constants' section and Extended Data Table 4). In particular, simple dimensionless frequency ratios, $\mathcal{R}_{a,b} = f_a/f_b$, can be formed that exhibit no dependence on R_∞, as well as a reduced sensitivity to μ/m_e whose fractional uncertainty would otherwise be important ($u_r(\mu/m_e|_{\text{Penning}}) = (3.1–4.6) \times 10^{-11}$, depending on the data source). Table 2 presents the favourable ratios $\mathcal{R}_{5,1}$ and $\mathcal{R}_{9,5}$. Modified, dimensional frequency combinations can further reduce the uncertainty arising from $\mu/m_e|_{\text{Penning}}$, in view of the smallness of other uncertainty contributions. This comes at the expense of

reintroducing a small sensitivity to R_∞. The indicated $\mathcal{R}_{5,1}'^{(\text{theor})}$ and $\mathcal{R}_{9,5}'^{(\text{theor})}$ are the combinations of f_1, f_5 and f_5, f_9 with the smallest uncertainty.

The ratios are mostly sensitive to the non-relativistic energy contributions as well as the lower-order QED effects (Table 2, rows 11–15). The ratios are sensitive to hypothetical additional terms in the Schrödinger equation, for example, a local self-interaction term proportional to the squared wavefunction. Thus, the comparison between the experimental and theoretical ratios can be used to bound the strength of such terms (Supplementary Information). Finally, the ratios are relatively insensitive to a Yukawa-type fifth force (Extended Data Fig. 2).

We find that the experimental and theoretical values of ratios $\mathcal{R}$ (Table 2) agree within the combined uncertainties. We propose

$$\Delta_{5,1}' = (\mathcal{R}_{5,1}'^{(\text{exp})} - \mathcal{R}_{5,1}'^{(\text{theor})})/\mathcal{R}_{5,1} \tag{4}$$

as a metric for the test of quantum physics of a system where the motion and interaction of two baryons are the dominant aspects. With the present experiment, we achieve $\Delta_{5,1}' = -3.0(4.2) \times 10^{-12}$. Other metrics, such as $\Delta_{9,5}'$, have a similar fractional uncertainty. The numerical results depend on the assumed correlation between QED uncertainties (see 'Frequency combinations with reduced sensitivity to fundamental constants' section). Implications of the results are given below.

(II) It has been proposed that standard quantum mechanics should be modified and must be described by a Lindblad density matrix evolution. Weinberg[6] explored the consequences for atomic clocks and found that the observed transition frequencies ν_{ij} may be shifted from the energy differences $(E_i - E_j)/h$ by amounts described by unknown parameters ε_{ij}. He suggested that the shifts may be tested for atoms by measuring three transitions within a subset of three 'clock'-type levels 1, 2 and 3, and testing whether the transition frequencies ν_{12}, ν_{23} and ν_{13} violate the 'closure' $\nu_{12} + \nu_{23} \neq \nu_{13}$. We pointed out that MHI are suitable systems for such a test because each isotopologue provides hundreds of rovibrational levels, and a multitude of transitions having small natural linewidth and small systematic effects may be found[16]. Examples are the three levels $(v, N) = (0, 0)$, $(1, 1)$ and $(5, 1)$ mentioned here, but more have been discussed theoretically[17–20]. Here we argue that calculable systems (MHI, hydrogen-like atoms and so on) permit a direct test of Weinberg's hypothesis: the difference between an experimental transition frequency $\nu_{ij}^{(\text{exp})}$ and the (conventionally computed) theoretical transition frequency $\nu_{ij}^{(\text{theor})} = (E_j^{(\text{theor})} - E_i^{(\text{theor})})/h$ yields a value for ε_{ij}. From equations (2) and (6), we find $\varepsilon_5/f_5 = 0.1(2.1) \times 10^{-11}$. Furthermore, the frequency ratios introduced above provide the parameter combination $\varepsilon_5/f_5 - \varepsilon_1/f_1 = (\mathcal{R}_{5,1}^{(\text{exp})} - \mathcal{R}_{5,1}^{(\text{theor})})/\mathcal{R}_{5,1} \simeq -3.7(5.2) \times 10^{-12}$. Obviously, this is a significant bound only if the parameters ε_{ij} do not have the property of scaling linearly or approximately linearly with f_{ij}. Both results find no evidence for Weinberg's hypothesis.

(III) The comparison of the value of μ/m_e from this work with the value obtained from the Penning trap results can be considered as a test for deviations from quantum theory, specifically for systems involving baryonic motion. The relevant data are m_e/u from CODATA 2018 (a value that relies mostly on another work[21], where electron spin resonance of C$_5^+$ was measured), m_p/u (ref. [22]), m_d/u (ref. [23]) and m_d/m_p (ref. [24]). Indeed, these Penning trap experiments were operated such that the motion of the employed baryonic or baryon-containing particles (C$_5^+$, proton, deuteron, H$_2^+$ and HD$^+$) was in the classical regime, unlike the quantized motion of baryons in HD$^+$. Note that the electron in the HD$^+$ molecule as well as in the C$_5^+$ ion are in quantum motion. The four (independent) Penning trap measurements can be combined in three ways to form $\mu/m_e|_{\text{Penning}}$ values. These three values are consistent with each other (Extended Data Table 3 reports two such values). The present HD$^+$ result and the most accurate value resulting from m_e/u, m_d/u and m_d/m_p (Extended Data Table 3, row 22) exhibit a moderate tension of $1.7\sigma_{\text{tot}}$, where σ_{tot} is the combined uncertainty.

Table 2 | Ratios $\mathcal{R}$ of spin-averaged transition frequencies, measured and calculated ab initio

Name	$\mathcal{R}_{5,1}$	$\mathcal{R}'_{5,1}$	$\mathcal{R}_{9,5}$	$\mathcal{R}'_{9,5}$	Row
Ratio	f_5/f_1	$f_5/f_1^{0.87}$	f_9/f_5	$f_9/f_5^{0.86}$	
Experiment	4.432433066069	111.2945104411	1.598630181280	63.35615636157	1
Fractional uncertainty	3.5×10^{-12}	3.2×10^{-12}	2.6×10^{-12}	2.3×10^{-12}	2
Theory	4.432433066085	111.2945104415	1.598630181287	63.35615636184	3
Theoretical fractional uncertainty due to					
QED theory	2.6×10^{-12}	2.6×10^{-12}	2.5×10^{-12}	2.5×10^{-12}	4
Spin theory	4.3×10^{-13}	3.8×10^{-13}	2.4×10^{-13}	2.3×10^{-13}	5
R_∞ (CODATA18)	0	2.0×10^{-13}	0	3.0×10^{-13}	6
μ/m_e (CODATA18)	3.0×10^{-12}	5.0×10^{-14}	3.0×10^{-12}	5.0×10^{-13}	7
r_p, r_d (CODATA18)	1.0×10^{-13}	2.0×10^{-13}	9.0×10^{-14}	3.0×10^{-13}	8
(Exp.−Theory)/Exp.	**−3.7×10⁻¹²**	**−3.0×10⁻¹²**	−4.4×10⁻¹²	−4.3×10⁻¹²	9
u(Exp.−Theory)/Exp.	**5.2×10⁻¹²**	**4.2×10⁻¹²**	4.8×10⁻¹²	3.4×10⁻¹²	10
Theoretical fractional contributions due to					
Nuclear charge radii	9.0×10^{-11}	-1.9×10^{-10}	7.5×10^{-11}	-2.2×10^{-10}	11
$O(\alpha^2)$ including nuclear charge radii	-1.7×10^{-6}	5.4×10^{-7}	-1.8×10^{-6}	3.7×10^{-7}	12
$O(\alpha^3)$	1.8×10^{-7}	-3.8×10^{-7}	1.5×10^{-7}	-4.2×10^{-7}	13
$O(\alpha^4)$	1.2×10^{-9}	-2.8×10^{-9}	9.5×10^{-10}	-3.1×10^{-9}	14
$O(\alpha^5)$	-6.6×10^{-11}	1.8×10^{-10}	-5.3×10^{-11}	2.0×10^{-10}	15
$O(\alpha^6)$	5.3×10^{-14}	-1.6×10^{-12}	9.3×10^{-14}	-1.7×10^{-12}	16
Other	-1.8×10^{-13}	4.0×10^{-13}	-1.5×10^{-13}	4.5×10^{-13}	17
$d(\ln \mathcal{R}_{i,j})/d(\ln(m_p/m_e))$	4.1×10^{-2}	-6.7×10^{-4}	4.7×10^{-2}	7.5×10^{-3}	18
$d(\ln \mathcal{R}_{i,j})/d(\ln(m_d/m_e))$	2.1×10^{-2}	-3.4×10^{-4}	2.3×10^{-2}	3.7×10^{-3}	19

The unprimed ratios are dimensionless, whereas the primed ratios $\mathcal{R}'_{m,n}$ are dimensional and weakly dependent on R_∞. The omitted unit for the numbers in column 3, row 1 and column 3, row 3 is kHz$^{0.13}$, and that for the numbers in column 5, row 1 and column 5, row 3 is kHz$^{0.14}$. The main result is indicated in bold typeface. In rows 6–8, the uncertainties due to different fundamental constants are individually given, without considering the correlations between the constants. The fractional uncertainties of the theoretical spin frequency values applied to the experimental frequencies are not included in row 2, but are listed in row 5. In the total fractional uncertainty of the experiment-to-theory comparison (row 10), correlations between the uncertainties of the fundamental constants have been ignored, since they do not substantially alter the result. The lower half of the table (rows 11–19) presents the fractional contributions of various energy contributions to the theoretical ratios, as well as the normalized sensitivities to the mass ratios. The spin theory uncertainty is calculated assuming that the hyperfine theory uncertainties of the individual frequencies are not correlated, whereas for the QED theory uncertainty, a correlation coefficient $r_{QED}=0.95$ is assumed. We verified that the correlations of the hyperfine coefficients' uncertainties do not notably change the experimental ratios and total spin theory uncertainty.

The uncertainty of the HD⁺ result is 1.5 times smaller than the Penning trap result (Extended Data Fig. 3).

The extended transition frequency set $\{f_0, f_1, f_5, f_9\}$ enables a more powerful analysis compared with using a single frequency. Using a least-squares adjustment (LSA), we fit or adjust constants so that the theoretical predictions $f_i^{(theor)}$ match the experimental results $f_i^{(exp)}$. An LSA with the previously available three frequencies, namely, f_0', f_1' and f_9' (differing from the present values), was reported in another work[2]. As stated, here we mostly consider the pair f_1 and f_5. First, we note that the LSA of R_∞, μ/m_e and r_p with data only from HD⁺ spectroscopy, and not from (muonic) hydrogen spectroscopy, yields large uncertainties because of the dependencies of f_i on R_∞ and r_p are in part similar (Supplementary Section A). A simple LSA (LSA-1 (Supplementary Section A) and part (a) in Table 3) consists of fitting only the value of μ/m_e to the f_1 and f_5 HD⁺ data, with constants from (muonic) hydrogen spectroscopy included parametrically. This results in

$$\mu/m_e|_{LSA1} = 1,223.899228713(23). \qquad (5)$$

The value and uncertainty are constrained by the near-unity QED uncertainty correlation $r_{QED} = 0.95$, and therefore, no notable reduction in uncertainty occurs compared with the uncertainties obtained when considering individual measurements (Extended Data Table 3). The value in equation (5) remains in moderate tension with the Penning trap result (Extended Data Fig. 3). Extended Data Table 5 and Extended Data Fig. 3 provide details on an LSA including f_0.

(IV) We set bounds to the strength of an assumed BSM force. We assume a Yukawa-type BSM potential[25], $V_Y(\Lambda_s, R_s) = 2\beta_s \exp(-R_s/\Lambda_s)/R_s$, where β_s is the strength, and R_s is the distance between any two particles (s = pd, ep and ed) and Λ_s is the range of the potential, both in units of Å. The frequency shifts caused by this type of potential are computed by perturbation theory (see 'BSM force' section). For the range $\Lambda_s = 0.15–0.25$ Å, the bounds from different vibrational transitions are complementary to each other. Among the ratios, we find that $\mathcal{R}_{5,0}$ is the most sensitive to β_{pd}, whereas $\mathcal{R}_{9,5}$ and $\mathcal{R}'_{9,5}$ are more than one order less sensitive around $\Lambda_{pd} = 0.4$ Å. Taking into account the uncertainties of the frequencies as well as frequency ratios (Extended Data Tables 3 and 4), we compute the bounds on β_{pd} at various assumed Λ_{pd} values (Fig. 3). We recognize that $\mathcal{R}_{5,0}$ is a more valuable metric than the individual frequencies for $0.13 < \Lambda_{pd} < 0.34$ Å. Also, $\mathcal{R}_{5,0}$ is independent of R_∞, and is weakly sensitive to the uncertainties of r_p and r_d, but its value depends on the mass ratio and QED corrections. Thus, we must interpret an $\mathcal{R}_{5,0}$-derived bound on β_{pd} as being related to BSM physics that allows for a BSM force, but respects conventional quantum physics for baryon and electron motion.

Furthermore, for setting a bound to β_{pd}, it is reasonable to fit β_{pd} and simultaneously adjust or fit μ/m_e. One reason for doing so is that the precision of HD⁺ spectroscopy is higher than that of the Penning trap measurements. Fitting both quantities (LSA-2) allows to simultaneously test for unconventional physics via both a BSM force and a different behaviour of baryons in quantum motion compared with classical motion. LSA-4 weakens the influence of the latter test. LSA-2

Table 3 | Two LSAs of fundamental constants

(a)	Constant X	$X_{LSA-1} - X_{CODATA18}$	$u_{r,LSA-1}$	$u_{r,CODATA18}$	$u_{r,Penning}$
	μ/m_e	$(-1.0 \pm 2.3) \times 10^{-8}$	1.8×10^{-11}	4.6×10^{-11}	3.1×10^{-11}

(b)	X	$X_{LSA-2} - X_{CODATA18}$	$u_{r,LSA-2}$	$u_{r,CODATA18}$	$u_{r,Penning}$
	μ/m_e	$(-5.6 \pm 6.5) \times 10^{-8}$	5.3×10^{-11}	4.6×10^{-11}	3.1×10^{-11}
	R_∞	$(0 \pm 2.1) \times 10^{-5} \, m^{-1}$	1.9×10^{-12}	1.9×10^{-12}	
	r_p	$(0 \pm 1.9) \times 10^{-3} \, fm$	2.3×10^{-3}	2.3×10^{-3}	
	β_{pd}	$(4.6 \pm 6.2) \times 10^{-12} E_h$	–	–	

In both parts (a) and (b), column 3 gives the result of the adjusted constants or parameters listed in column 2. Their fractional uncertainty is reported in column 4. For comparison, column 5 shows the CODATA 2018 fractional uncertainties, and column 6 shows the fractional uncertainties of the Penning trap measurements. The analysis is based on the two HD$^+$ transition frequencies f_1 and f_5 (equation (5)). (a) LSA-1 (equation (5)) probes unconventional physics that expresses itself in a value of the baryon–electron mass ratio μ/m_e different in the baryon quantum motion regime from that exhibited by the classical motion of baryonic particles. If we assume conventional physics to hold, as implied by the inclusion of CODATA constants as pseudo-data, then LSA-1 determines the baryon–electron mass ratio μ/m_e with 1.7 times higher accuracy than Penning trap experiments. (b) LSA-2 tests for non-standard physics via μ/m_e and β_{pd} with the strength of an additional Yukawa-type potential. A concrete example of a Yukawa potential range $\Lambda_{pd,0}$ is shown, chosen to be substantially larger than the equilibrium internuclear distance $R_{pd,eq}$, that is, $\Lambda_{pd,0} = 7.9$ Å. In neither LSA-1 nor LSA-2, the CODATA value for μ/m_e is included in the pseudo-data. Hydrogen data are, however, taken into account via the CODATA 2018 values of other constants, and therefore, conventional leptonic physics is assumed to hold. An exception is the uncertainty of $\Delta r_{pd'}^2$ which is not taken into account in LSA-2. Each HD$^+$ frequency data uncertainty includes the QED theory uncertainty, assumed to be strongly correlated among the four predictions[2], at a level of $r_{QED} = 0.95$ (see 'Ab initio theory of transition frequency' section), whereas the experimental uncertainties and spin theory uncertainties are assumed to be uncorrelated. It was verified that neglecting the spin theory correlations does not substantially impact the result. The uncertainty of μ/m_e from Penning trap determinations (column 6) results from the data in other work[14,23,24]. Here E_h denotes the Hartree energy.

and LSA-4 are performed with some CODATA 2018 values included as pseudo-data. Part (b) in Table 3 shows the LSA-4 result for a particular Λ_{pd}. Figure 3 (orange) reports the LSA-2 bound for variable Λ_{pd}.

We now compare the above test results with other state-of-the-art tests for baryons and other particles, beyond the Penning trap experiments mentioned above.

Neutral hydrogen molecules contain the same baryons as the MHI. The best agreements between theory and experiment are at the level of 5×10^{-9} for H$_2$ and D$_2$, more than two orders weaker than here[26].

Atom interferometry determines the mass of an atom species assuming standard quantum mechanics for the atomic motion to hold. In one of the most accurate experiments so far[27], the mass of rubidium (in kg) was measured with a relative uncertainty of 1.4×10^{-10}. This mass (in kg) is also measured by mass spectrometry[28], with fractional uncertainty essentially given by that of the atomic mass unit, $u_r(1 \, u) = 3 \times 10^{-10}$. Thus, the wave mechanics of the atomic motion is verified in the quoted interferometry experiment at this level. However, currently, the disagreement with a previous experiment[29] is larger than this level.

For the neutron[30], gravity resonance spectroscopy has jointly tested the quantum motion and gravitational interaction at the 1% level. From a comparison of experimental and theoretical data, neutron–nucleus scattering length bounds for a scalar internuclear BSM force can be set. The agreement at the 10^{-4} level leads to tight bounds, for example, $|\alpha_G| \leq 1 \times 10^{23}$ for $\Lambda = 1$ Å.

Antiprotonic helium is a system in which the motion of the helium nucleus, a baryon, considerably contributes to the internal energy. The combined results of spectroscopy of antiprotonic helium with 8×10^{-10} precision[31], of antihydrogen and Penning trap tests of the equality of the mass-to-charge ratios of antiproton and proton at a level of 1.6×10^{-11} (ref. 32) can be interpreted as a combined test of the low-energy quantum physics of the α particle and an antimatter baryon at the 8×10^{-10} level.

For electrons, the most accurate measurements are possible on the hydrogen atom. The uncertainty of R_∞ may be viewed as the accuracy
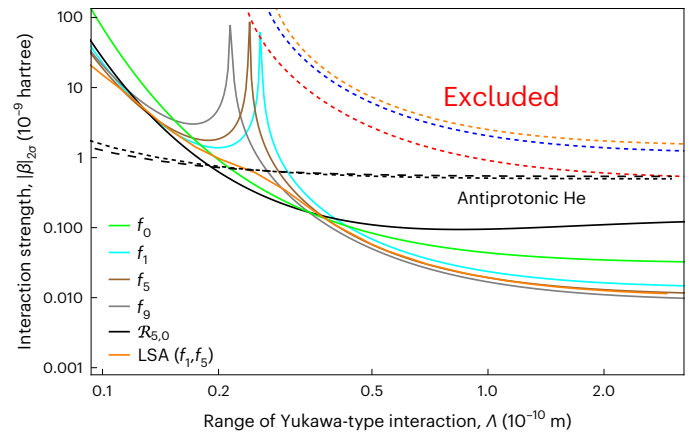

Fig. 3 | Bounds to the strength of a BSM proton–deuteron Yukawa-type interaction. The 2σ bound for $|\beta_{pd}|$ derived from LSA-4 based on f_1 and f_5 (orange). In LSA-4, β is fitted and μ/m_e is adjusted, that is, $\mu/m_e|_{(CODATA2018)}$ is included as pseudo-data. The other five full lines are bounds derived, in turn, from the four individual frequencies as well as from the frequency ratio $\mathcal{R}_{5,0} = f_5/f_0$. These five bounds are solely based on $f_i^{(exp)} - f_i^{(theor)}|_{(CODATA2018)}$ or $\mathcal{R}_{5,0}^{(exp)} - \mathcal{R}_{5,0}^{(theor)}|_{(CODATA2018)}$, fitting β without any adjustment of constants. Also, $|\beta|_{2\sigma}$ denotes the larger of the absolute values of the 2σ confidence interval limits for β_{pd}. All the bounds apply to the proton–deuteron interaction under the following conditions. (1) For ranges $\Lambda < 0.2$ Å, a BSM electron–nucleus interaction is weaker than the BSM proton–deuteron interaction by several orders. (2) For $\Lambda > 2$ Å, the former interaction should be at least one order smaller. In both cases, equal interaction ranges Λ_{pd}, Λ_{ep} and Λ_{ed} between different particles are assumed. The bounds set by earlier experiments are shown as dashed curves, namely, red[35], blue[36] and orange[37]. Also shown are bounds for the antiproton–α particle interaction: black long-dashed and black short-dashed curves indicate two different transitions[38]. Other analyses are discussed elsewhere[3,5,39].

of low-energy quantum theory involving electron motion. Implicitly, this also contains a test of the electron–proton interaction, particularly for ranges comparable with the Bohr radius (experiments on Rydberg states of the hydrogen atom probe moderately larger scales). CODATA has currently assigned R_∞ an uncertainty of 1.9×10^{-12} (ref. 14). However, this level is attained by including the results of muonic hydrogen spectroscopy, systems that involve the wave mechanics of a different lepton. The same behaviour for the muon and electron (lepton universality) needs to be assumed if the above uncertainty is to be assigned to a test of electron physics. Instead, if we consider only the spectroscopy results based on the electron, the uncertainty is larger, approximately 5×10^{-12} (Fig. 1 in ref. 14). This is comparable with the uncertainty for the present test based on HD$^+$, an observation that motivates further work towards higher accuracy also on the hydrogen system.

If we assume that either there are no deviations from conventional electron physics (as also suggested by g-factor determinations) and conventional electron–baryon interaction or that lepton universality holds, then our present study can be considered more specifically to be a verification of baryonic quantum motion and baryon–baryon interaction, at a level of $u(\Delta_{5,1}') \simeq 4.1 \times 10^{-12}$. Without these assumptions, tests based on HD$^+$ must be considered as combined tests of baryonic and electronic low-energy quantum physics.

We see potential for improvement of the test based on the frequency ratios $\mathcal{R}'_{m,n}$ to the 1×10^{-12} level by further improving experimental accuracy. Furthermore, a global data analysis testing for the existence of BSM forces, treating both lepton and baryon sectors on an equal footing, is a desirable major endeavour. The first study in this direction has recently been presented[33].

Online content

Any methods, additional references, Nature Portfolio reporting summaries, source data, extended data, supplementary information,

References

1. Caswell, W. & Lepage, G. Effective Lagrangians for bound state problems in QED, QCD, and other field theories. *Phys. Lett. B* **167**, 437–442 (1986).
2. Korobov, V. I. & Karr, J.-P. Rovibrational spin-averaged transitions in the hydrogen molecular ions. *Phys. Rev. A* **104**, 032806 (2021).
3. Alighanbari, S., Giri, G. S., Constantin, F. L., Korobov, V. I. & Schiller, S. Precise test of quantum electrodynamics and determination of fundamental constants with HD+ ions. *Nature* **581**, 152–158 (2020).
4. Kortunov, I. V. et al. Proton–electron mass ratio by high-resolution optical spectroscopy of ion ensembles in the resolved-carrier regime. *Nat. Phys.* **17**, 59–573 (2021).
5. Germann, M. et al. Three-body QED test and fifth-force constraint from vibrations and rotations of HD+. *Phys. Rev. Research* **3**, L022028 (2021).
6. Weinberg, S. Lindblad decoherence in atomic clocks. *Phys. Rev. A* **94**, 042117 (2016).
7. Blythe, P., Roth, B., Fröhlich, U., Wenz, H. & Schiller, S. Production of ultracold trapped molecular hydrogen ions. *Phys. Rev. Lett.* **95**, 183002 (2005).
8. Hornekær, L., Kjærgaard, N., Thommesen, A. M. & Drewsen, M. Structural properties of two-component Coulomb crystals in linear Paul traps. *Phys. Rev. Lett.* **86**, 1994–1997 (2001).
9. Kondov, S. S. et al. Molecular lattice clock with long vibrational coherence. *Nat. Phys.* **15**, 1118–1122 (2019).
10. Amitay, Z., Zajfman, D. & Forck, P. Rotational and vibrational lifetime of isotopically asymmetrized homonuclear diatomic molecular ions. *Phys. Rev. A* **50**, 2304–2308 (1994).
11. Karr, J.-P., Haidar, M., Hilico, L., Zhong, Z.-X. & Korobov, V. I. Higher-order corrections to spin-spin scalar interactions in HD+ and H_2^+. *Phys. Rev. A* **102**, 052827 (2020).
12. Korobov, V. I., Karr, J.-P., Haidar, M. & Zhong, Z.-X. Hyperfine structure in the H_2^+ and HD+ molecular ions at order ma^6. *Phys. Rev. A* **102**, 022804 (2020).
13. Korobov, V. I. & Karr, J.-P. Spin–orbit interaction in the HD+ ion. *Eur. Phys. J. D* **76**, 197 (2022).
14. Tiesinga, E., Mohr, P. J., Newell, D. B. & Taylor, B. N. CODATA recommended values of the fundamental physical constants: 2018. *Rev. Mod. Phys.* **93**, 025010 (2021).
15. Haidar, M., Korobov, V. I., Hilico, L. & Karr, J.-P. Higher-order corrections to the spin-orbit and spin-spin tensor interactions in HD+. *Phys. Rev. A* **106**, 042815 (2022).
16. Raizen, M. G., Gilbert, G. & Budker, D. Proposed test of quantum mechanics with three connected atomic clock transitions. *Phys. Rev. A* **106**, 032209 (2022).
17. Karr, J.-P. H_2^+ and HD+ : candidates for a molecular clock. *J. Mol. Spectrosc.* **300**, 37–43 (2014).
18. Schiller, S., Bakalov, D. & Korobov, V. I. Simplest molecules as candidates for precise optical clocks. *Phys. Rev. Lett.* **113**, 023004 (2014).
19. Bakalov, D. & Schiller, S. The electric quadrupole moment of molecular hydrogen ions and their potential for a molecular ion clock. *Appl. Phys. B* **114**, 213–230 (2014).
20. Korobov, V. I., Danev, P., Bakalov, D. & Schiller, S. Laser-stimulated electric quadrupole transitions in the molecular hydrogen ion H_2^+. *Phys. Rev. A* **97**, 032505 (2018).
21. Köhler, F. et al. The electron mass from *g*-factor measurements on hydrogen-like carbon $^{12}C^{5+}$. *J. Phys. B: At. Mol. Opt. Phys.* **48**, 144032 (2015).
22. Heiße, F. et al. High-precision mass spectrometer for light ions. *Phys. Rev. A* **100**, 022518 (2019).
23. Rau, S. et al. Penning trap mass measurements of the deuteron and the HD+ molecular ion. *Nature* **585**, 43–47 (2020).
24. Fink, D. J. & Myers, E. G. Deuteron-to-proton mass ratio from simultaneous measurement of the cyclotron frequencies of H_2^+ and D+. *Phys. Rev. Lett.* **127**, 243001 (2021).
25. Salumbides, E., Ubachs, W. & Korobov, V. Bounds on fifth forces at the sub-Å length scale. *J. Mol. Spectrosc.* **300**, 65–69 (2014).
26. Czachorowski, P., Puchalski, M., Komasa, J. & Pachucki, K. Nonadiabatic relativistic correction in H_2, D_2, and HD. *Phys. Rev. A* **98**, 052506 (2018).
27. Morel, L., Yao, Z., Cladé, P. & Guellati-Khélifa, S. Determination of the fine-structure constant with an accuracy of 81 parts per trillion. *Nature* **588**, 61–65 (2020).
28. Mount, B. J., Redshaw, M. & Myers, E. G. Atomic masses of ^6Li, ^{23}Na, $^{39,41}K$, $^{85,87}Rb$, and ^{133}Cs. *Phys. Rev. A* **82**, 042513 (2010).
29. Parker, R. H., Yu, C., Zhong, W., Estey, B. & Müller, H. Measurement of the fine-structure constant as a test of the Standard Model. *Science* **360**, 191–195 (2018).
30. Sponar, S., Sedmik, R. I. P., Pitschmann, M., Abele, H. & Hasegawa, Y. Tests of fundamental quantum mechanics and dark interactions with low-energy neutrons. *Nat. Rev. Phys.* **3**, 309–327 (2021).
31. Hori, M. et al. Buffer-gas cooling of antiprotonic helium to 1.5 to 1.7 K, and antiproton-to–electron mass ratio. *Science* **354**, 610–614 (2016).
32. Borchert, M. J. et al. A 16-parts-per-trillion measurement of the antiproton-to-proton charge-mass ratio. *Nature* **601**, 53–57 (2022).
33. Delaunay, C. et al. Self-consistent extraction of spectroscopic bounds on light new physics. *Phys. Rev. Lett.* **130**, 121801 (2023).
34. Patra, S. et al. Proton-electron mass ratio from laser spectroscopy of HD+ at the part-per-trillion level. *Science* **369**, 1238–1241 (2020).
35. Biesheuvel, J. et al. Probing QED and fundamental constants through laser spectroscopy of vibrational transitions in HD+. *Nat. Commun.* **7**, 10385 (2016).
36. Koelemeij, J. C. J., Roth, B., Wicht, A., Ernsting, I. & Schiller, S. Vibrational spectroscopy of HD+ with 2-ppb accuracy. *Phys. Rev. Lett.* **98**, 173002 (2007).
37. Bressel, U. et al. Manipulation of individual hyperfine states in cold trapped molecular ions and application to HD+ frequency metrology. *Phys. Rev. Lett.* **108**, 183003 (2012).
38. Hori, M. et al. Two-photon laser spectroscopy of antiprotonic helium and the antiproton-to-electron mass ratio. *Nature* **475**, 484–488 (2011).
39. Hollik, W. G., Linster, M. & Tabet, M. A study of New Physics searches with tritium and similar molecules. *Eur. Phys. J. C* **780**, 661 (2020).

Methods

Apparatus

The experimental apparatus used in the present work has been employed in previous spectroscopy experiments[3,4,40], but the spectroscopy laser source is replaced with a continuous-wave, high-power diode laser emitting at 1.15 μm. The laser is stabilized to a reference cavity and steered to a hydrogen maser on long timescales. In more detail, the laser is phase locked to a femtosecond fibre frequency comb, which is itself phase locked to an ultrastable 1.06 μm laser (reference laser 1). The phase-locked beats are constantly monitored and display sub-hertz linewidths. Extended Data Fig. 1 (left, blue trace in the inset) shows one of the two beats. The linewidth of the spectroscopy laser is, to a large extent, determined by the linewidth of reference laser 1. To characterize the latter, we obtained a direct beat between reference laser 1 and an independent reference laser 2 (also at 1.06 μm), frequency locked to its own ultrastable cavity. This reference laser 2 has sub-hertz linewidth and low frequency drift. The beat note (Extended Data Fig. 1, left, red trace) exhibits a full-width at half-maximum smaller than 3 Hz. Furthermore, the spectral transfer noise of the comb was determined in a separate experiment to be less than 2 Hz. The frequency noise occurring in the fibre connecting the comb and spectroscopy laser was measured to contribute approximately 4 Hz. We, therefore, infer that altogether, the linewidth of the spectroscopy laser wave is approximately 10 Hz.

The absolute optical frequency f of the spectroscopy laser is calculated in real time by measuring the repetition rate of the frequency comb and the carrier-envelope offset frequency with two frequency counters and the phase-locked-loop beats with spectrum analysers. The counters and spectrum analysers are referenced to a hydrogen maser (maser 1). A second hydrogen maser (maser 2), nominally identical to maser 1, verifies the stability of maser 1 (Extended Data Fig. 1, right, green trace). The slow frequency drift of the spectroscopy laser frequency of the order of 0.1 Hz min^{-1} (Extended Data Fig. 1, right, red trace for long averaging times) is actively compensated with a digital servo. The frequency instability of the spectroscopy laser frequency (Allan deviation) is less than 2×10^{-14} on all timescales. More precisely, for integration times smaller than 10 s, the instability is similar to the values given by the red curve, namely, $\leq 5 \times 10^{-15}$. Because of the drift of the reference cavity of reference laser 1 (to which the comb is locked), on long timescales (>200 s), the spectroscopy laser frequency is steered to the maser 1 frequency via the frequency comb. Extended Data Fig. 1 (right, blue trace) shows that this steering is effective: the blue trace drops below the red trace and does not exceed the green trace. For these long integration times, the Allan deviation of the spectroscopy laser is similar to the values of the green trace that indicate the instability of maser 1. Thus, the laser reaches an instability of 2×10^{-15} for integration times of the order of 1 h. The blue data (laser versus maser) are limited on short timescales (≤10 s) by the instability of maser 1 and the resolution of the frequency counter. The slight increase in the values for integration times of 80 to 200 s is probably due to a sub-optimal performance of the digital servo on this timescale.

The state preparation and destructive spectroscopy sequence underlying the reported measurements are the variation of a previously described procedure[3,4]. Each measurement cycle starts with 35 s of rotational laser cooling[41] to increase the population in the ground state ($v = 0, N = 0$). This consequently improves the signal-to-noise ratio. The first secular excitation (application of an RF voltage having a frequency close to the secular frequency $\omega \simeq 2\pi \times 800$ kHz to an electrode close to the trap, for 6 s) produces a signal proportional to the number of HD$^+$ ions in the trap. Then, the 1.15 μm spectroscopy laser and 266 nm photodissociation laser are applied for a total of 4 s, allowing vibrational excitation with REMPD of HD$^+$ ions to take place. To avoid a systematic shift induced by the 266 nm photodissociation laser, we employed a sequence of interleaved 1.15 μm and 266 nm irradiations during the REMPD. Since the excited state ($v' = 5, N' = 1$) has

a lifetime of ~16 ms (ref. 10), we used fast optical shutters. The 1.15 μm and 266 nm laser pulse durations are 10 ms each and there was a delay of 100 μs between the two pulses. This sequence is repeated 190 times.

The sequence is followed by a second secular excitation of the same duration as the first. Then, a 4 s interval follows, during which only the photodissociation laser is applied as the spectroscopy laser is blocked. A third secular excitation is then applied. From the change in fluorescence levels caused by the first two secular excitations, the fractional decrease in the number of HD$^+$ ions due to laser vibrational excitation is computed, representing the spectroscopy plus background signal, whereas the last two secular excitations yield the background loss of ions. This determination of the background loss immediately after REMPD is different from how the background ion loss was determined in our previous works[3,4]. For each frequency detuning of the spectroscopy laser, the measurement cycle is repeated until adequate statistics is accumulated.

Systematic shifts

We measured several systematic effects (Table 1).

(1) A systematic frequency shift caused by the trap RF electric field is present. It may be due to the a.c. Stark shift and/or the a.c. Zeeman shift[3]. The measurement of the transition frequency for three different RF amplitudes (Fig. 2a(i),(ii)) allowed for an extrapolation to zero amplitude. The extrapolated value is compared with the value at our nominal operational RF amplitude (Table 1).

(2) We measured the transition frequency for three values of magnetic field $B < 1 \times 10^{-4}$ T (Fig. 2b(i),(ii)). Assuming the predicted quadratic-in-B scaling, an extrapolation to $B = 0$ was performed. The zero-field transition frequency offset from the frequency at the nominal magnetic field (3×10^{-5} T) is indicated as the d.c. Zeeman shift.

(3) The laser wave for beryllium-ion laser cooling (30–40 μW at 313 nm) and the spectroscopy wave potentially cause light shifts (a.c. Stark shifts) via the polarizability of the molecular ion. We measured the combined light shifts induced by these two waves by simultaneously increasing the respective laser powers by a factor of two (Fig. 2c(i),(ii)). This measurement determines a combined a.c. Stark effect correction. We find it to be consistent with zero within our resolution. The photodissociation laser (~30 mW at 266 nm) is not applied during the spectroscopy.

(4) An upper bound for the d.c. Stark shift was determined by measuring the transition frequency, once with the nominal trap operating conditions (when the spectroscopy HD$^+$-ion string is located along the symmetry axis of the Be$^+$ ion cluster) and again with an additional d.c. voltage of 5 V applied on two trap electrodes[3]. In the latter case, the Be$^+$ ion cluster is visibly displaced by approximately 100 μm, and leaves the HD$^+$-ion string undisplaced. The current experimental resolution does not allow to resolve the frequency shift (Fig. 2d(i),(ii)). As the applied displacement is large, we assign a zero correction to the transition frequency and an uncertainty equal to the statistical uncertainty of the line centre determination.

(5) The sensitivity of all the transition frequencies to external fields can be computed ab initio. This includes Zeeman shift[42], electric quadrupole shift[19], black-body radiation shift, spin-state-dependent d.c. Stark shift and light shift[43]. The quadratic Zeeman shift coefficients for the components $m_F = 0 \rightarrow m'_F = 0$ of line 12 and line 21 amount to -0.38 and -0.43 MHz mT^{-2}, respectively. The experimental shifts are consistent with this prediction. The light shift of the lower and upper vibrational levels due to radiation of any wavelength can be computed from the

measured laser intensities and the theoretical polarizabilities provided by theory[43]. We quote only the scalar (subscript s) and tensor (subscript t) polarizabilities, because the vector polarizability is not relevant for states having $m_F = 0$.

For the lower level ($v = 0$, $N = 0$), the polarizabilities for 313 nm have already been given elsewhere[3]:
$\alpha_s(v = 0, N = 0, \lambda = 313$ nm$) = 3.496$, $\alpha_t(v = 0, N = 0, \lambda = 313$ nm$) = 0$. At the wavelength of 266 nm, the polarizabilities are $\alpha_s(v = 0, N = 0, \lambda = 266$ nm$) = 3.677$, $\alpha_t(v = 0, N = 0, \lambda = 266$ nm$) = 0$.

For the upper level, they are $\alpha_s(v' = 5, N' = 1, \lambda = 313$ nm$) = -17.61$, $\alpha_t(v' = 5, N' = 1, \lambda = 313$ nm$) = 8.855$, $\alpha_s(v' = 5, N' = 1, \lambda = 266$ nm$) = 11.89$ and $\alpha_t(v' = 5, N' = 1, \lambda = 266$ nm$) = -8.876$.

These values are in atomic units. For the different spin transitions, correction factors of the order of 1 need to be applied. For the employed nominal laser intensities, we compute transition frequency shifts of <1 Hz due to the 313 nm wave intensity and <80 Hz in magnitude for the 30 mW, 266 nm wave having the given beam waist parameter. However, the latter wave is blocked during vibrational excitation.

The transition frequency has a black-body radiation shift of f_5 (300 K) − f_5(0 K) = -1.2×10^{-16} (ref. [43]).

The electric quadrupole shift is negligible.

(6) The hydrogen maser frequency offset is determined by a common-view global navigation satellite system technique. A correction of 1.4646(7) kHz was applied to the frequency values measured with respect to the maser.

(7) The present measurement can only be reasonably matched with theory if the measured frequency is corrected for the recoil shift. Given the HD$^+$ mass and the wavelength of transition, the applied correction is −49.58 kHz, and its uncertainty is negligible. We undertook additional experimental studies that give robust evidence for the recoil shift when the transition wavelength is short, by performing absolute frequency measurements of one hyperfine component of two other rovibrational transitions. To uncover any dependence on the wave propagation direction of the spectroscopy, we aligned the wave along the trap axis rather than orthogonal to it. We addressed the (0, 1)→(5, 0) and (0, 0)→(4, 1) transitions at 1,165 nm and 1,404 nm, respectively. In both cases, we observed a sub-Doppler peak and the difference between the measured optical frequency and ab initio predicted value was consistent with the occurrence of a corresponding recoil shift. Furthermore, we have measured the thermally broadened line of the studied hyperfine component of the (0, 1)→(5, 0) transition. The linewidth observed under our operating conditions corresponds, according to our molecular dynamics (MD) simulations, to an ion temperature of approximately 1 mK, a value substantially smaller than that assumed previously[3]. For this temperature, the MD simulations predict a Dicke-narrowed peak of substantial strength relative to the thermally broadened line. These MD simulations are fully classical, however, and are not suited to investigate the issue of a recoil shift, which is a quantum effect. A theory explaining the appearance of the recoil is not available yet. Nevertheless, we believe that an important aspect that such a theory must take into account is that the mixed ion cluster exhibits many vibrational modes of frequencies comparable and even smaller than the recoil frequency, and that are thermally excited.

Thus, aside the recoil shift, the most important systematic shift exhibited by the spectroscopy apparatus is the trap-shift effect. For either line, the total applied correction, excluding maser correction and recoil shift, is less than 0.7 kHz in magnitude. It is consistent with zero, the total uncertainty being approximately 0.9 kHz.

(8) The total uncertainty includes the statistical uncertainty of the nominal transition frequencies. For every measured transition line in Fig. 2, we have assigned one-half of the fitted full width as statistical uncertainty of the line centre frequency.

(9) For the fundamental vibrational transition f_1 (ref. [4]), we assume that no recoil shift (2.5 kHz) occurs. If it did and the corresponding correction were included, a significant contradiction with theory would appear, namely, $\Delta'_{5,1} = 34(4.1) \times 10^{-12}$. A tentative explanation for the absence of recoil shift is that the number of modes having comparable or smaller frequency than the recoil is much smaller than in the case of f_5 photon absorption. Furthermore, for the abovementioned low temperature of the ion cluster, the large transition wavelength ($\lambda_1 = 5.1$ μm) and the transverse spectroscopy wave propagation, our MD simulations show that the Lamb–Dicke regime is attained, that is, $2\pi x_{r.m.s.}(T = 0.9$ mK$)/\lambda_1 \simeq 0.6$. Here, $x_{r.m.s.}$ is the root mean square displacement of the HD$^+$ ions of the string in a direction transverse to the trap axis.

Ab initio theory of transition frequency

The problem of computing the energy of a rovibrational state of the HD$^+$ molecule in its ground electronic state is divided into the computation of the level energy averaged over all the possible spin states of the contributing particles, that is, $E_{spin-avg}(v, N)$, and the additional energies $E_{spin}(v, N, p = (G_1, G_2, F))$ related to the non-zero particle magnetic moments. The transition frequency between two particular spin states p and q of two rovibrational states is then the sum of the energy differences, that is, $hf^{(theor)}_{line\,i} = f^{(theor)}_{spin-avg} + f^{(theor)}_{spin,i} = E^{(theor)}_{spin-avg}(v', N') - E^{(theor)}_{spin-avg}(v, N) + E^{(theor)}_{spin,q}(v', N') - E^{(theor)}_{spin,p}(v, N)$, with the line number $i = i(p, q)$ (Extended Data Fig. 4 provides the nomenclature).

(1) The ab initio spin-averaged frequency has been evaluated as

$$f^{(theor)}_5 = f^{(theor)}_{spin-avg} = 259,762,971,051.0(2.1)_{theor,QED}(5.1)_{CODATA2018} \text{ kHz}.$$
(6)

Extended Data Table 2 provides details on $f^{(theor)}_{spin-avg}$. The first uncertainty results from an estimate of the unevaluated QED contributions. The second uncertainty arises from the fundamental constants that are needed as inputs to the theoretical prediction. Since approximately $f_5 \propto R_\infty \sqrt{m_e/\mu}$, where $\mu = m_p m_d/(m_p + m_d)$ is the reduced nuclear mass (see 'Frequency combinations with reduced sensitivity to fundamental constants' section), the current uncertainty of the electron–proton mass ratio, $u(m_e/m_p|_{CODATA2018})$ (ref. [14]), makes the dominant contribution, that is, 4.4 kHz. The uncertainties of R_∞ and proton and deuteron charge radii together contribute 0.3 kHz.

(2) The value and uncertainty of several results in this work, for example, $\Delta'_{5,1}$ and $\Delta'_{9,5}$ (equation (5)), depend on the assumed level of correlation between the QED uncertainties of the individual theoretical transition frequencies. A high level of correlation has been argued for in the ab initio theory work[2,5,44]. Assuming perfect correlation (correlation coefficient $r_{QED} = 1$), the chi-squared test for LSA-1 indicates a possible inconsistency in the data. If the assumption is slightly relaxed, for example, to $r_{QED} = 0.95$, the indication is removed. We have used this value in the present work.

(3) The functional dependence of the spin-averaged frequency on μ/m_e is calculated ab initio as $\partial \ln f^{(theor)}_{spin-avg}(\mu/m_e)/\partial \ln(\mu/m_e) \simeq -0.422544$; it is close to the Born–Oppenheimer value of $-\frac{1}{2}$.

(4) The hyperfine structure in each rovibrational level is described by an effective Hamiltonian[45], containing terms proportional to nine coefficients $\varepsilon_1(v, N), \ldots, \varepsilon_9(v, N)$. Their values depend on the rovibrational level (v, N). For $N = 0$ levels, only the Fermi contact interaction coefficients ε_4 and ε_5 are non-zero. Although these

coefficients could, in principle, be experimentally determined, the current state of the art has not yet achieved this. Therefore, we rely on their accurate theoretical calculation. Recently, $\mathcal{E}_4$ and $\mathcal{E}_5$ for many rovibrational levels have been computed[11] with account of all the contributions of order α^2, and their fractional uncertainty is of the order of α^3, or $u_{4,\mathrm{r}}, u'_{4,\mathrm{r}} \simeq 9 \times 10^{-7}$ and $u_{5,\mathrm{r}}, u'_{5,\mathrm{r}} \simeq 6 \times 10^{-7}$ (unprimed and primed quantities refer to $(v = 0, N = 0)$ and $(v' = 5, N' = 1)$, respectively). The coefficient $\mathcal{E}'_1$ (third in magnitude after $\mathcal{E}'_4$ and $\mathcal{E}'_5$) as well as $\mathcal{E}'_6$ and $\mathcal{E}'_7$ have also been recently theoretically computed with reduced theory uncertainty of $u'_{1,\mathrm{r}} \simeq 3 \times 10^{-6}$ and $u'_{6,\mathrm{r}}, u'_{7,\mathrm{r}} \simeq 2 \times 10^{-6}$ (refs. 13,46). The remaining spin coefficients $\mathcal{E}'_2$, $\mathcal{E}'_3, \mathcal{E}'_8$ and $\mathcal{E}'_9$ have been computed within the Breit–Pauli approximation. This neglects terms of relative order α^2; therefore, we assume that their fractional uncertainties are equal to α^2. The spin frequencies $f_{\mathrm{spin},i}^{(\mathrm{theor})}$ are computed by diagonalizing the effective Hamiltonian. Also, their sensitivity to the various spin coefficients can be numerically evaluated; they are denoted by $\gamma_{i,k}, \gamma'_{i,k}$. Extended Data Table 1 reports all the relevant quantities. According to theoretical considerations[13], there are significant correlations between the uncertainties of the coefficients $\mathcal{E}_k$. In particular, near-perfect correlation is expected between the uncalculated theory contributions of $\mathcal{E}_2(v, N)$ and $\mathcal{E}_3(v, N)$, $\mathcal{E}_6(v, N)$ and $\mathcal{E}_7(v, N)$, $\mathcal{E}_4(v, N)$ and $\mathcal{E}_4(v', N')$, and $\mathcal{E}_5(v, N)$ and $\mathcal{E}_5(v', N')$. This results in

$$f_{\mathrm{spin},12}^{(\mathrm{theor})} = -56,675.71(6)_{\mathrm{theor,spin}} \text{ kHz},$$
$$f_{\mathrm{spin},21}^{(\mathrm{theor})} = 69,416.31(7)_{\mathrm{theor,spin}} \text{ kHz}. \tag{7}$$

The small spin theory uncertainties are a result of the correlations between the Hamiltonian coefficients. Note that these spin theory uncertainties are substantially smaller than the uncertainty of the spin-averaged frequency (equation (7)).

In the present study, a test of the spin theory is provided by the measured separation of the two hyperfine lines. The experimental result and theoretical prediction are

$$f_{\mathrm{line21}}^{(\mathrm{exp})} - f_{\mathrm{line12}}^{(\mathrm{exp})} = 126,092.6(1.2)_{\mathrm{exp}} \text{ kHz},$$
$$f_{\mathrm{spin,21}}^{(\mathrm{theor})} - f_{\mathrm{spin,12}}^{(\mathrm{theor})} = 126,092.0(0.1)_{\mathrm{theor,spin}} \text{ kHz}. \tag{8}$$

Note that we have computed the theory uncertainty of the spin frequency difference using the values $\gamma_{21,k} - \gamma_{12,k}$ and $\gamma'_{21,k} - \gamma'_{12,k}$. This good agreement can be viewed as a test of spin structure theory that is complementary to our previous test on the fundamental vibrational transition[4]. In that test, one hyperfine structure splitting was measured as $41,294.06(32)_{\mathrm{exp}}$ kHz and the prediction is $41,293.66(12)_{\mathrm{theor,spin}}$ kHz (theory re-evaluated using another work[13]). Although that agreement is more precise than in the present work, the two spin transitions shared the same lower state, which is not the case in this work.

Composite frequency

From each experimental rovibrational line frequency, we can subtract the corresponding theoretical spin frequency and obtain a spin-averaged rovibrational frequency. From two such values, we can also form a linear combination (composite frequency) as

$$f_{\mathrm{spin-avg}}^{(\mathrm{exp})} = b_{12}\left(f_{\mathrm{line12}}^{(\mathrm{exp})} - f_{\mathrm{spin,12}}^{(\mathrm{theor})}\right) + (1 - b_{12})\left(f_{\mathrm{line21}}^{(\mathrm{exp})} - f_{\mathrm{spin,21}}^{(\mathrm{theor})}\right), \tag{9}$$

where the weight b_{12} is arbitrary. We may choose it such that the total uncertainty—experimental combined with spin theory—is minimized. The optimum value is $b_{12} \simeq 0.49$, giving a spin theory uncertainty of 0.035 kHz (an LSA yields the same result). Note that this is smaller by a factor of two than the individual spin theory uncertainties (equation (7)), and is again a result of the correlations among the Hamiltonian

coefficients. The composite frequency does not appreciably change if the correlations are neglected.

Frequency combinations with reduced sensitivity to fundamental constants

Extended Data Table 4 gives a number of frequency ratios and Table 2 is a subset. We note the following features.

(1) The particle masses directly affect the vibrational transition frequencies, in the combination $\mu/m_\mathrm{e} = m_\mathrm{p} m_\mathrm{d}/m_\mathrm{e}(m_\mathrm{p} + m_\mathrm{d})$. This is reflected in a nearly exact 2:1 ratio of the sensitivities of the transition frequencies to the proton–electron and deuteron–electron mass ratios[47] (Extended Data Table 3, rows 18 and 19). Because of the anharmonicity of the effective nuclear molecular potential, the transition frequency for a given pair of vibrational levels does not scale precisely as $(m_\mathrm{e}/\mu)^{1/2}$, the dependence found in the Born–Oppenheimer approximation. The logarithmic sensitivity of the frequencies is smaller than 1/2, moderately decreasing with increasing upper-level quantum number v'. As a result, frequency ratios maintain, in general, a sensitivity to μ/m_e, but reduced by a factor of up to approximately 20, as evident by comparing row 8 in Extended Data Table 3 and row 7 in Extended Data Table 4. Consequently, $u_\mathrm{r}(\mu/m_\mathrm{e}|_{\mathrm{CODATA2018}}) \simeq 5 \times 10^{-11}$ contributes, for example, a 3×10^{-12} fractional uncertainty of the ratios $\mathcal{R}_{5,1}$ and $\mathcal{R}_{9,5}$. This is further reduced in ratios of suitably chosen powers of frequencies, for example, to 5×10^{-14} in $\mathcal{R}'_{5,1}$. Note that such ratios are dimensional, and therefore, their numerical values are not of fundamental importance.

(2) All the transition frequencies are proportional to R_∞, known today with 2×10^{-12} fractional uncertainty[48]. However, by considering frequency ratios $\mathcal{R}_{a,b}^{(\mathrm{theor})} = f_a^{(\mathrm{theor})}/f_b^{(\mathrm{theor})}$, this uncertainty becomes negligible. This also holds for $\mathcal{R}'^{(\mathrm{theor})}_{9,5}$.

(3) The contributions from nuclear, relativistic and from QED effects scale, for vibrational transitions, approximately linearly with the transition frequency (Extended Data Table 3, rows 11–17). This implies that their fractional contributions to frequency ratios $\mathcal{R}$ are substantially reduced, by approximate factors of 10–100. We note that this is actually reflected in the presented values of $\mathcal{R}^{(\mathrm{theor})}$ only because the Bethe logarithm, which contributes at fractional order α^3, has been calculated with fractional uncertainty smaller than 1×10^{-7} (ref. 49); therefore, its uncertainty affects the transition frequency only at the level of 1×10^{-12} or lower. The said reduction in the ratios also occurs for the most relevant contributions in this respect, namely, the QED contributions of the next-highest (α^5) and of the highest (α^6) computed order so far, which are the ones that contribute most to the uncertainty of the individual transition frequencies[2]. The corresponding reduction factor is ~20. Finally, concerning the so far uncalculated QED contributions of higher order, Korobov and Karr argued that the corresponding uncertainties of different transition frequencies are fully correlated (see 'Ab initio theory of transition frequency' section). Then, the frequency ratios $\mathcal{R}$ have a QED-theory fractional uncertainty (rows 4 in Table 2 and Extended Data Table 4) smaller than that of the individual frequencies f, the latter standing at 8×10^{-12} for vibrational transitions[2].

(4) The uncertainty originating from the proton and deuteron charge radii impacts the transition frequencies at the 2×10^{-12} fractional level; this decreases more than tenfold in some frequency ratios (rows 8 in Table 2 and Extended Data Table 4).

(5) The 'pure' vibrational transition frequency $f_{\mathrm{spin-avg}}$, computed ab initio, cannot be directly measured. Rather, any particular experimentally measured rovibrational transition is a particular

hyperfine component i and its frequency $f_{\text{line }i}$ is the sum of $f_{\text{spin-avg}}$ and a hyperfine (spin) frequency $f_{\text{spin},i}$, of the order of 10 MHz (see 'Ab initio theory of transition frequency' section). Experimental values of $f_{\text{line }i}$ can be corrected by subtracting the ab initio $f_{\text{spin},i}^{(\text{theor})}$ value, at the cost of introducing theory uncertainty. With the most recent improvements in hyperfine structure theory[13] (see 'Ab initio theory of transition frequency' section), the corresponding uncertainties $u\left(f_{\text{spin},i}^{(\text{theor})}\right)$ have been reduced to a level substantially smaller than the QED uncertainty.

BSM force

The effect of a weak BSM force between the proton and deuteron with arbitrary R_{pd} dependence on a spin-averaged transition frequency can be computed by the first-order perturbation theory as $h\Delta f_{v,N\to v',N'}(\{\lambda\}) = \langle V_5(\{\lambda\}, R_{\text{pd}})\rangle_{v',N'} - \langle V_5(\{\lambda\}, R_{\text{pd}})\rangle_{v,N}$, where $V_5 \propto \beta_{\text{pd}}$ is the BSM potential and $\{\lambda\}$ are additional parameters of the potential. The individual expectation values of the potential, $\langle V_5\rangle_{v,N}$, are computed with respect to the nuclear vibrational wavefunction of the rovibrational level (v, N). Korobov computed the shifts for the commonly considered case of a Yukawa potential as $V_5 = V_Y$, characterized by a range $\{\lambda\} = \Lambda_{\text{pd}}$. The effect of a BSM force on ratios $\mathcal{R}$ is obtained by computing the effect on each individual frequency $f_{v,N\to v',N'}$ appearing in the ratio. The sensitivity of various frequency ratios $\mathcal{R}$ and various frequencies f to the strength β_{pd} of the proton–deuteron potential V_Y is presented in Extended Data Fig. 2a. The four transition frequencies $f_{v'}$ are affected in different ways.

Similarly, we can consider weak BSM forces between the electron and proton (ep) or electron and deuteron (ed). Again, we require expectation values such as $V_5(\{\lambda\}, R_{\text{ep}})\rangle_{v,N}$ in case that the BSM force depends only on the electron–proton distance R_{ep}. Their calculation has been done with respect to the full Schrödinger wavefunction of the three-body problem in a given rovibrational level. These wavefunctions have three arguments, namely, distances R_{ep}, R_{ed} and R_{pd}. Extended Data Fig. 2b shows the sensitivities of a Yukawa-type potential $V_Y(\Lambda_{\text{ep}}, R_{\text{ep}}) \propto \beta_{\text{ep}}$ to strength β_{ep}, as a function of the assumed range Λ_{ep}. Because of the equal charge of the proton and deuteron and the small mass of the electron compared with the nuclear masses, the wavefunction is nearly symmetric with respect to R_{ep} and R_{ed} (Born–Oppenheimer approximation), and therefore, the sensitivities to β_{ep} and β_{ed} are nearly equal.

A comparison of Extended Data Fig. 2a,b shows that the sensitivities to electron–nucleus BSM forces are not negligible compared with the case of a proton–deuteron BSM force, for any (same) range Λ_s. In fact, they are larger in magnitude for the range $\Lambda_s < 0.3$ Å, whereas in the limit of ranges exceeding the proton–deuteron equilibrium distance $R_{\text{pd,eq}} = 1.06$ Å, the sensitivities of all the transitions to the three types of force (pd, ep and ed) are similar. Here $\mathcal{R}_{5,0}$ is only moderately less sensitive to the electron–nucleus BSM forces than to the proton–deuteron force (Extended Data Fig. 2a,b, black lines).

This implies that an encompassing test for BSM forces should include electron–nucleus BSM forces in the analysis[5,39]. However, HD$^+$ spectroscopy data alone are, at present, insufficient to allow an analysis that tests for β_{pd}, β_{ep} and β_{ed}, as well as adjusts R_∞, μ/m_e, r_p and r_d. If atomic hydrogen results are included in the analysis to provide inputs for R_∞, r_p and r_d, then for consistency, the effect of electron–nucleus BSM forces (β_{ep}, β_{ed}) on hydrogen frequencies must be treated[50,51]. Such an endeavour is beyond the scope of this work. Therefore, for simplicity, we shall assume $\beta_{\text{ep}} = \beta_{\text{ed}} = 0$. Bounds to β_{pd} can then be set from the ratios $\mathcal{R}$ or via LSA.

Bounds for β_{pd} can be translated to those for the often considered coupling parameter α_G that establishes the BSM potential strength relative to gravity via $\alpha_G = 2(\beta_{\text{pd}} \times 10^{-10} \text{ m})/(G_N m_p m_d)$, where G_N is the gravitational constant. For $\Lambda_{\text{pd}} = 1$ Å, the bound from LSA-2 is $|\alpha_G|_{2\sigma} < 8.2 \times 10^{25}$.

Mass ratios from f_5

From our μ/m_e in equation (3), we can determine the proton–electron mass ratio by using the value of m_d/m_p determined by the most accurate Penning trap experiment[24] as

$$m_p/m_e = 1,836.152673463(10)_{\text{exp}}(35)_{\text{theor,QED}}$$
$$(1)_{\text{theor,spin}}(6)_{\text{CODATA2018,Fink-Myers}}, \tag{10}$$

with the total fractional uncertainty $u_r = 2.0 \times 10^{-11}$. This value is consistent with the ratio obtained from the atomic masses of electron[14] and proton[22], that is, 1,836.152673390(81), but is two times more accurate.

Furthermore, using the value m_d/u (ref. 23), we obtain the electron mass $m_e/u = 5.48579909030(12) \times 10^{-4}$; it exhibits moderate tension compared with the CODATA 2018 value, the difference being $-3.5(2.0)_{\text{tot}} \times 10^{-14}$.

Data availability

Source data are available for this paper. All other data that support the plots within this paper and other findings of this study are available from the corresponding author upon reasonable request.

Code availability

No custom code or software was used for analysis and presentation of the data associated with this paper.

References

40. Alighanbari, S., Hansen, M. G., Korobov, V. I. & Schiller, S. Rotational spectroscopy of cold and trapped molecular ions in the Lamb–Dicke regime. *Nat. Phys.* **14**, 555 (2018).
41. Schneider, T., Roth, B., Duncker, H., Ernsting, I. & Schiller, S. All-optical preparation of molecular ions in the rovibrational ground state. *Nat. Phys.* **6**, 275–278 (2010).
42. Bakalov, D., Korobov, V. & Schiller, S. Magnetic field effects in the transitions of the HD$^+$ molecular ion and precision spectroscopy. *J. Phys. B: At. Mol. Opt. Phys.* **44**, 025003 (2011).
43. Schiller, S., Bakalov, D., Bekbaev, A. K. & Korobov, V. I. Static and dynamic polarizability and the Stark and blackbody-radiation frequency shifts of the molecular hydrogen ions H$_2^+$, HD$^+$, and D$_2^+$. *Phys. Rev. A* **89**, 052521 (2014).
44. Karr, J.-P., Hilico, L., Koelemeij, J. C. J. & Korobov, V. I. Hydrogen molecular ions for improved determination of fundamental constants. *Phys. Rev. A* **94**, 050501 (2016).
45. Bakalov, D., Korobov, V. I. & Schiller, S. High-precision calculation of the hyperfine structure of the HD$^+$ ion. *Phys. Rev. Lett.* **97**, 243001 (2006).
46. Haidar, M. *Hyperfine Structure in the Hydrogen Molecular Ions.* PhD thesis, Univ. Sorbonne (2021).
47. Schiller, S. & Korobov, V. Test of time-dependence of the electron and nuclear masses with ultracold molecules. *Phys. Rev. A* **71**, 032505 (2005).
48. Tiesinga, E., Mohr, P. J., Newell, D. B. & Taylor, B. N. *Values of Fundamental Physical Constants* https://physics.nist.gov/cuu/Constants/index.html (2019).
49. Korobov, V. I. & Zhong, Z.-X. Bethe logarithm for the H$_2^+$ and HD$^+$ molecular ions. *Phys. Rev. A* **86**, 044501 (2012).
50. Kloor, H., Fischbach, E., Talmadge, C. & Greene, G. L. Limits on new forces coexisting with electromagnetism. *Phys. Rev. D* **49**, 2098–2113 (1994).
51. Karshenboim, S. G. Precision physics of simple atoms and constraints on a light boson with ultraweak coupling. *Phys. Rev. Lett.* **104**, 220406 (2010).

Acknowledgements

Competing interests

The authors declare no competing interests.

Additional information

Extended data is available for this paper at https://doi.org/10.1038/s41567-023-02088-2.

Supplementary information The online version contains supplementary material available at https://doi.org/10.1038/s41567-023-02088-2.

Correspondence and requests for materials should be addressed to S. Schiller.

Peer review information *Nature Physics* thanks Piotr Wcislo and the other, anonymous, reviewer(s) for their contribution to the peer review of this work.

Reprints and permissions information is available at www.nature.com/reprints.
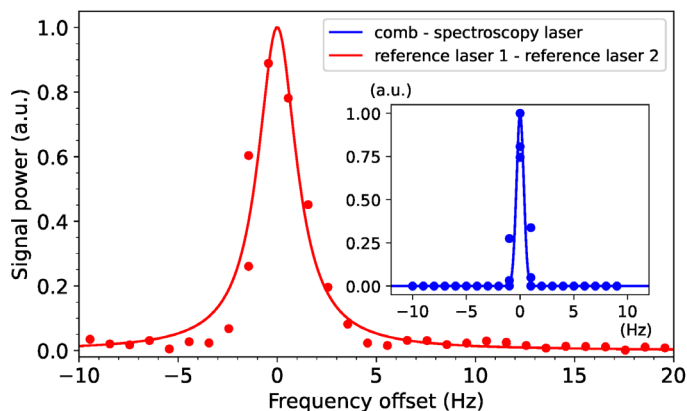
Extended Data Fig. 1 | Spectral characteristics of the 1.15 μm spectroscopy laser. Left: (red) spectrum analyzer trace of the heterodyne beat of the reference laser 1 (1.06 μm) and an independent sub-Hz-linewidth, low-drift frequency-stable laser of nearly same optical frequency (reference laser 2, 1.06 μm); (inset, blue) the heterodyne beat between the spectroscopy laser and the spectrally closest mode of the frequency comb, while the spectroscopy laser is phase-locked to the comb and the comb is phase-locked to the reference laser 1. The solid lines are the lorentzian fits to the data points. The frequency offsets are arbitrary. The linewidths of the two beats and additional characterizations indicate that the spectroscopy laser has a linewidth of less than 10 Hz. Resolution bandwidth of the spectrum analyzer: 1 Hz, red trace - single sweep, sweep time 6 s, blue trace - average of 10 sweeps, time span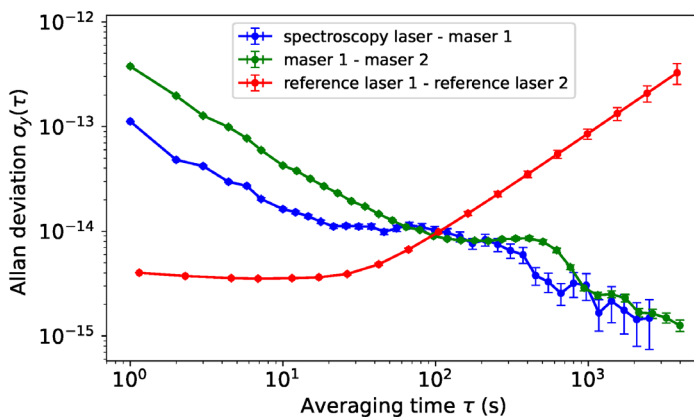 of 1 min. The error bars are smaller than data markers. **Right**: (blue) Allan deviation of the frequency of the spectroscopy laser, measured relative to a hydrogen maser (maser 1) via the frequency comb; (green) Allan deviation of maser 1 relative to a second independent maser (maser 2). The shown values are the Allan deviation of the beat frequency divided by $\sqrt{2}$; (red) Allan deviation of the beat of the reference laser 1 with reference laser 2. The error bars are estimated as 68% confidence intervals.
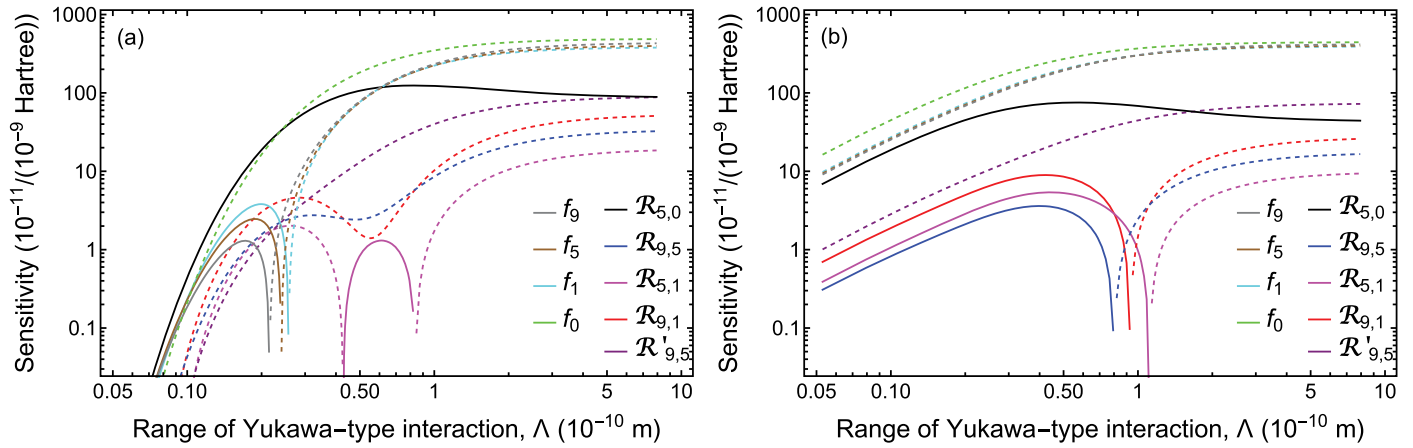
Extended Data Fig. 2 | Sensitivity of transitions and their ratios to BSM forces. The sensitivity is defined as $X^{-1}(dX/d\beta)$, where $X = f_{v'}$ or $\mathcal{R}_{a,b}$, and is computed as described in Methods, Sec. 1.5. β has units of energy. **(a)**: case of a BSM force between proton and deuteron, proportional to β_{pd}. **(b)**: case of a BSM force between electron and proton, proportional to β_{ep}. Full lines denote positive values, dashed lines negative values. The brown, cyan, and gray lines in panel (b) are very close.
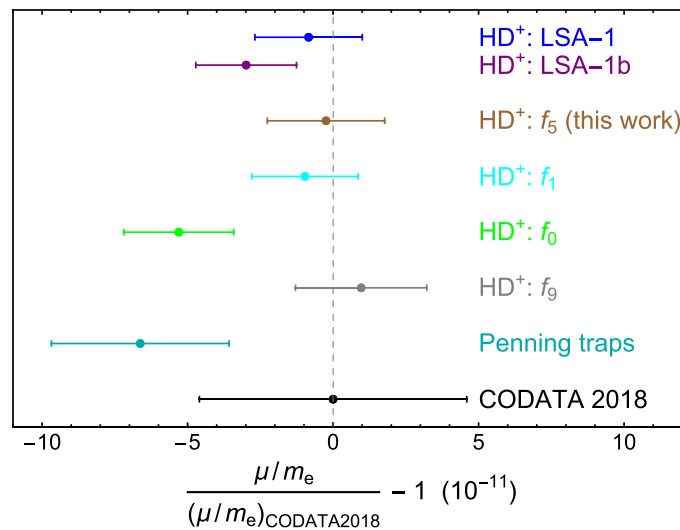
Extended Data Fig. 3 | Comparison of results on the fundamental mass ratio μ/m_e. $\mu = m_p m_d/(m_p + m_d)$ is the reduced proton-deuteron mass. "Penning traps" (dark cyan): computed using the CODATA 2018 value for m_e/u (that relies mostly on ref. [21]), m_d/u[23], m_d/m_p[24]. CODATA 2018 (black): μ/m_e computed using only the CODATA values for m_e/u, m_p/u, m_d/u. The vertical line corresponds to zero of x axis. Note that the value and uncertainty of the "CODATA 2018" entry is significantly correlated with the "Penning traps" entry. LSA-1 is based on f_1 (cyan) and f_5 (brown); LSA-1b is based on f_0 (green), f_1 (cyan) and f_5 (brown). LSA-1b and LSA-3 (ED Table 5) are nearly identical. As can be seen, the results of the least-squares adjustments deviate from the respective weighted means of the included frequencies. This is due to the assumption of near-perfect correlation r_{QED} of the theoretical uncertainties. The error bars represent standard uncertainty.
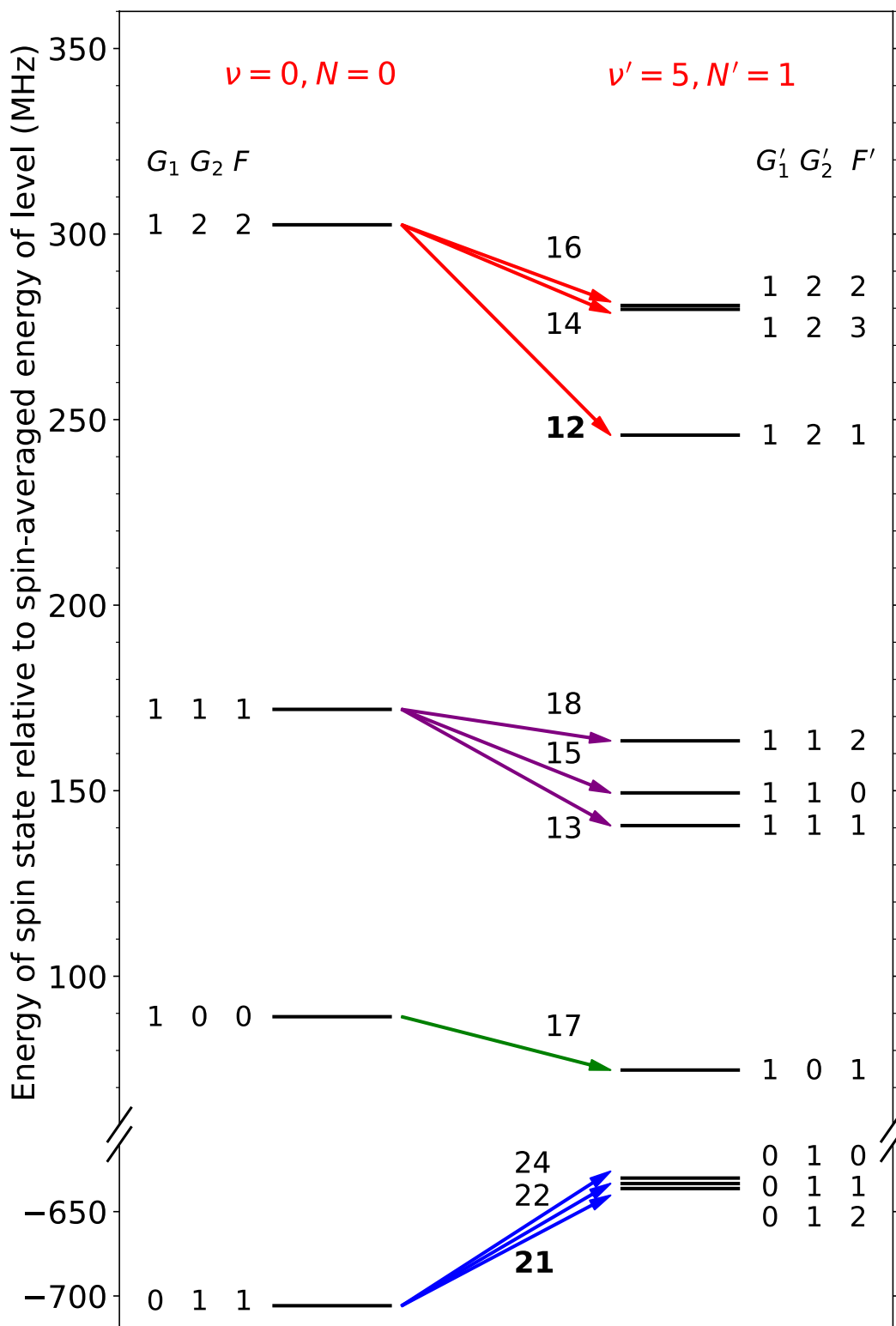
Extended Data Fig. 4 | Hyperfine structure energy levels of HD⁺ in the two relevant rovibrational levels. Shown are the values $E_{\text{spin},p}^{(\text{theor})}/h$ for the ground vibrational level ($v = 0, N = 0$) (left) and $E_{\text{spin},q}^{(\text{theor})}/h$ for the excited vibrational level ($v' = 5, N' = 1$) (right) of the $^2\Sigma_g^+$ ground electronic state. The vertical axis is broken for better visualization. The numbers next to the arrows indicate the line numbers $i(p, q)$, where $p(q)$ denotes the particular lower (upper) spin state. In this work, line 12 and line 21 were measured. G_1 refers to the sum of electron and proton spin, G_2 to the sum of G_1 and deuteron spin, and F to the sum of G_2 and rotational angular momentum N. The ground rovibrational level has zero rotational angular momentum, $N = 0$, giving rise to 4 spin states with total

angular momentum $F = 0, 1, 2$. The upper rovibrational level ($v' = 5, N' = 1$) has 10 spin states, having values $F' = 0, 1, 2, 3$. For both studied lines 12 and 21, the lower and upper hyperfine states have the same particle spin coupling $G_1 = G_1'$ and $G_2 = G_2'$. The line 12 measured here is analogous to line 12 in ref. 3 and to line 12 in ref. 4. The line 21 is analogous to line 16 in ref. 3. Spin states with total angular momentum F are $(2F + 1)$-fold degenerate in zero magnetic field. We denote the lines and corresponding transition frequencies in zero external fields by $f_{\text{line}i}$. i indicates the position in the list $\{f_{\text{spin},i}\}$ of the spin frequency values of all spin components in ascending order.

Extended Data Table 1 | Spin hamiltonian coefficients, spin structure frequencies, and spin frequency derivatives

		$\mathcal{E}_1{}'$	$\mathcal{E}_2{}'$	$\mathcal{E}_3{}'$	$\mathcal{E}_4{}'$	$\mathcal{E}_5{}'$	$\mathcal{E}_6{}'$	$\mathcal{E}_7{}'$	$\mathcal{E}_8{}'$	$\mathcal{E}_9{}'$	$\mathcal{E}_4$	$\mathcal{E}_5$
		24.07736	−0.02647	−0.004024	831.6874	127.93962	6.4214	0.98561	−0.002487	0.005346	925.3942	142.28756
Line i	$f_{\mathrm{spin},i}^{(\mathrm{theor})}$	$\gamma'_{i,1}$	$\gamma'_{i,2}$	$\gamma'_{i,3}$	$\gamma'_{i,4}$	$\gamma'_{i,5}$	$\gamma'_{i,6}$	$\gamma'_{i,7}$	$\gamma'_{i,8}$	$\gamma'_{i,9}$	$\gamma_{i,4}$	$\gamma_{i,5}$
12	−56.675711	−0.60080	−0.59205	−1.69934	0.24998	0.44737	−0.23030	−3.44936	−3.39148	−2.75290	0.25000	0.50000
21	69.416311	−0.10231	0.10686	0.99504	−0.73434	−0.18207	0.00884	0.13230	−0.14633	−0.49256	−0.73668	−0.16879

$\mathcal{E}'_k$ are the coefficients of the spin hamiltonian for the ($v' = 5, N' = 1$) level, in MHz. $\mathcal{E}_k$ are the coefficients for the rovibrational ground state ($v=0, N=0$), already reported in[3]. $f_{\mathrm{spin},i}^{(\mathrm{theor})}$ is the theoretical spin frequency in MHz, computed as in ref. [39]. The line number $i=i(p,q)$, where $p(q)$ denote the lower (upper) states. γ are the dimensionless sensitivities of the spin structure frequencies to the various spin Hamiltonian coefficients. $\gamma'_{i,k} = \partial f_{\mathrm{spin},i}^{(\mathrm{theor})}/\partial\mathcal{E}'_k$ refers to the upper state q, $\gamma_{i,k} = -\partial f_{\mathrm{spin},i}^{(\mathrm{theor})}/\partial\mathcal{E}_k$ to the lower state p.

Extended Data Table 2 | Contributions to the ab initio spin averaged frequency $f_5^{(theor)}$

relative order	value (kHz)
α^0	259 760 034 608.88
α^2	4 008 944.07
α^3	-1 065 424.00
α^4	-7 544.12
α^5	468.43
α^6	-3.39
other	1.11

The computation, using NRQED theory, follows refs. [2]. For the present transition frequency, a total of 41 individual contributions were calculated for both upper and lower rovibrational levels by V. I. Korobov. The relative order is relative to the transition frequency itself. The main contribution to $f_5^{(theor)}$ is the accurate solution of the non-relativistic three-body problem (relative order α^0). This is complemented by contributions that scale, relative to the main contribution, as the 2nd to 6th power of the fine-structure constant α. The term of relative order α^2 includes the effects of overlap of the electron's wavefunction with the finite-size proton and deuteron. These effects contribute $-70.0(3)_{CODATA18}$ kHz and $-465.9(3)_{CODATA18}$ kHz, respectively, to the transition frequency. We point out that the contribution of relative order α^6 includes also a recently calculated term that scales as $R_\infty \alpha^6 (\log \alpha^{-2})^2$, amounting to 10.02 kHz for the transition frequency. Additional contributions are from muon-antimuon and hadronic vacuum polarization in the electron propagator[2]. The fractional contributions are indicated in ED Table 1, column 2, rows 12 to 17.

Extended Data Table 3 | Properties of transitions that have been measured and calculated with high precision

Transition	$(0,0)\to(5,1)$	$(0,0)\to(0,1)$	$(0,0)\to(1,1)$	$(0,3)\to(9,3)$	row
Reference	this work	Alighanbari *et al.* (2020) (*)	Kortunov *et al.* (2021) (*)	Germann *et al.* (2021) (*)	
Experiment	f_5	f_0	f_1	f_9	1
frequency (kHz)	259762971051.24	1314925753.000	58605052164.19	415264925501.43	2
exp.unc.(frac., abs.)	2.3×10^{-12} , 0.60 kHz	1.2×10^{-11} , 0.015 kHz	2.6×10^{-12} , 0.15 kHz	1.1×10^{-12} , 0.46 kHz	3
Theory	f_5	f_0	f_1	f_9	4
frequency (kHz)	259762971050.97	1314925752.932	58605052163.92	415264925502.84	5
spin theory unc.(frac., abs.)	1.4×10^{-13} , 0.036 kHz	$2.\times10^{-12}$, 0.002 kHz	4.1×10^{-13} , 0.024 kHz	1.9×10^{-13} , 0.081 kHz	6
QED theory unc.(frac., abs.)	8.1×10^{-12} , 2.1 kHz	1.4×10^{-11} , 0.019 kHz	8.5×10^{-12} , 0.50 kHz	7.9×10^{-12} , 3.3 kHz	7
CODATA2018 unc.(frac., abs.)	1.9×10^{-11} , 5.1 kHz	4.6×10^{-11} , 0.061 kHz	2.2×10^{-11} , 1.3 kHz	1.6×10^{-11} , 6.6 kHz	8
Experiment − theory (kHz)	$0.27(5.5)_{tot}$	$0.069(0.066)_{tot}$	$0.27(1.4)_{tot}$	$-1.4(7.4)_{tot}$	9
frac. tot. unc.	2.1×10^{-11}	5.0×10^{-11}	2.4×10^{-11}	1.8×10^{-11}	10
theor. frac. contrib. from:					
nuclear radii	-2.1×10^{-9}	-3.6×10^{-9}	-2.2×10^{-9}	-2.0×10^{-9}	11
$O(\alpha^2)$ incl. nucl. radii	1.5×10^{-5}	3.7×10^{-5}	1.7×10^{-5}	1.4×10^{-5}	12
$O(\alpha^3)$	-4.1×10^{-6}	-7.1×10^{-6}	-4.3×10^{-6}	-4.0×10^{-6}	13
$O(\alpha^4)$	-2.9×10^{-8}	-5.0×10^{-8}	-3.0×10^{-8}	-2.8×10^{-8}	14
$O(\alpha^5)$	1.8×10^{-9}	3.0×10^{-9}	1.9×10^{-9}	1.8×10^{-9}	15
$O(\alpha^6)$	-1.3×10^{-11}	-1.2×10^{-11}	-1.3×10^{-11}	-1.3×10^{-11}	16
other	$4.\times10^{-12}$	$7.\times10^{-12}$	$4.\times10^{-12}$	$4.\times10^{-12}$	17
$d(\ln f)/d(\ln(m_p/m_e))$	-0.282	-0.658	-0.323	-0.235	18
$d(\ln f)/d(\ln(m_d/m_e))$	-0.141	-0.329	-0.162	-0.117	19
$\mu/m_e = m_p m_d/m_e(m_p+m_d)$					
HD$^+$ spectroscopy	1223.899228720(25)	1223.899228658(23)	1223.899228711(22)	1223.899228735(28)	20
CODATA 2018		1223.899228723(56)			21
Penning Traps		1223.899228642(37)			22

The frequency values $f_{v'}$ are spin-averaged frequencies. An experimental spin-averaged frequency is obtained by applying a theoretical spin frequency correction to data, and the resulting spin theory uncertainty is reported in row 8. Rows 11 to 17 shows the fractional relativistic and QED corrections computed perturbatively in different orders of the fine-structure constant. Rows 18 and 19 show the fractional sensitivities of the frequencies to the mass ratios. In the bottom section of the table the values of the normalized reduced nuclear mass are given, (i) determined from the individual HD$^+$ transition frequencies, (ii) reported by the CODATA2018 committee, (iii) deduced from Penning trap measurements. (*) The theoretical value of the $(0,0)\to(0,1)$ transition frequency has been updated compared to Ref. 3: $(f_0^{(theor)} - f_0^{(theor,prev)})/f_0 = 2.7\times10^{-11\,12}$. The experimental frequency has been corrected as follows: (1) correlations between the spin hamiltonian coefficient uncertainties are taken into account; (2) in view of the incomplete agreement between experimental and theoretical values of the frequencies of the spin components, a conservative reanalysis is made. The measured components lines 14 and 20 have the largest systematic corrections, mainly due to the Zeeman shift, and are therefore omitted. A fit of $f_{spin-avg}$, $\mathcal{E}_1(v=1,N=1)$ and $\mathcal{E}_6(v=0,N=1)$ is performed on the remaining four measured lines. The quality of the fit is very good. It results in shifts of $\mathcal{E}_1$ and $\mathcal{E}_6$ by −5.4±0.4 and −5.4±2.8 times their respective ab initio spin theory uncertainty. The composite frequency that eliminates the influence of $\mathcal{E}_1(v=0,N=1)$, $\mathcal{E}_6(v=0,N=1)$, $\mathcal{E}_7(v=0,N=1)$ yields the same result. For the $(0,0)\to(1,1)$ transition, the previous experimental value[4] has been updated $f_1^{(exp)} - f_1^{(exp,prev)} = -0.048$ kHz, due to an improved calculation of the spin frequencies[12] that are required as corrections. This reduction and the correction of an evaluation error are taken into account in the updated value of μ/m_e. No recoil correction has been introduced for the transition f_1, as currently no clear evidence has been seen (see 'Systematic shifts' section). The incomplete agreement between experimental and theoretical values of the frequencies of the spin components of the $(0,3)\to(9,3)$ transition has been noted before; nevertheless, we reevaluated the experimental transition frequency using the mentioned improved spin frequencies and their correlations, in the same way as for $f_1^{(exp)}$. The spin theory uncertainties were computed taking into account correlations between the hyperfine coefficients. In all columns, the uncertainty of the difference "Experiment - theory" is computed as r.m.s. of experimental, QED theory, spin theory, and CODATA2018 uncertainties. It is dominated by the CODATA2018 uncertainty. In the last section of the table, the uncertainty $u(\mu/m_e)$ for the value obtained from HD$^+$ spectroscopy is computed analogously. $u(\mu/m_e)$ for the Penning traps determination is computed from the uncertainties of the atomic mass of the electron[21] (modified as in[14]), of the atomic mass of the deuteron[23], and of the proton-deuteron mass ratio[24]. The transitions reported in previous work are from refs. 3–5.

Extended Data Table 4 | Ratios $\mathcal{R}$ of spin-averaged transition frequencies

name	$\mathcal{R}_{1,0}$	$\mathcal{R}_{5,0}$	$\mathcal{R}_{5,1}$	$\mathcal{R}'_{5,1}$	$\mathcal{R}_{9,1}$	$\mathcal{R}_{9,5}$	$\mathcal{R}'_{9,5}$	row
ratio	f_1/f_0	f_5/f_0	f_5/f_1	$f_5/f_1^{0.87}$	f_9/f_1	f_9/f_5	$f_9/f_5^{0.86}$	
Experiment	44.56909603486	197.5495349897	4.432433066069	111.2945104411	7.085821275920	1.598630181280	63.35615636157	1
frac. unc.	1.2×10^{-11}	1.2×10^{-11}	3.5×10^{-12}	3.2×10^{-12}	2.8×10^{-12}	2.6×10^{-12}	2.3×10^{-12}	2
Theory	44.56909603699	197.5495349999	4.432433066085	111.2945104415	7.085821275977	1.598630181287	63.35615636184	3
frac. unc. due to:								
QED theory	6.8×10^{-12}	7.1×10^{-12}	2.6×10^{-12}	2.6×10^{-12}	2.7×10^{-12}	2.5×10^{-12}	2.5×10^{-12}	4
spin theory	1.6×10^{-12}	1.6×10^{-12}	4.3×10^{-13}	3.8×10^{-13}	4.5×10^{-13}	2.4×10^{-13}	2.3×10^{-13}	5
R_∞ (CODATA18)	0	0	0	$2. \times 10^{-13}$	0	0	$3. \times 10^{-13}$	6
μ/m_e (CODATA18)	$2. \times 10^{-11}$	$3. \times 10^{-11}$	$3. \times 10^{-12}$	$5. \times 10^{-14}$	$6. \times 10^{-12}$	$3. \times 10^{-12}$	$5. \times 10^{-13}$	7
r_p (CODATA18) & r_d (CODATA18)	$2. \times 10^{-12}$	$2. \times 10^{-12}$	$1. \times 10^{-13}$	$2. \times 10^{-13}$	$2. \times 10^{-13}$	$9. \times 10^{-14}$	$3. \times 10^{-13}$	8
(Exp. − Theory)/Exp.	-4.8×10^{-11}	-5.1×10^{-11}	-3.7×10^{-12}	-3.0×10^{-12}	-8.1×10^{-12}	-4.4×10^{-12}	-4.3×10^{-12}	9
frac. unc. of (Exp. − Theory)	2.7×10^{-11}	2.9×10^{-11}	5.2×10^{-12}	4.2×10^{-12}	7.2×10^{-12}	4.8×10^{-12}	3.4×10^{-12}	10
theor. frac. contrib. from:								
nuclear radii	1.5×10^{-9}	1.5×10^{-9}	9.0×10^{-11}	-1.9×10^{-10}	1.6×10^{-10}	7.5×10^{-11}	-2.2×10^{-10}	11
$O(\alpha^2)$ inc. nucl. radii	-0.000020	-0.000021	-1.7×10^{-6}	5.4×10^{-7}	-3.5×10^{-6}	-1.8×10^{-6}	3.7×10^{-7}	12
$O(\alpha^3)$	2.8×10^{-6}	3.0×10^{-6}	1.8×10^{-7}	-3.8×10^{-7}	3.3×10^{-7}	1.5×10^{-7}	-4.2×10^{-7}	13
$O(\alpha^4)$	2.0×10^{-8}	2.1×10^{-8}	1.2×10^{-9}	-2.8×10^{-9}	2.1×10^{-9}	9.5×10^{-10}	-3.1×10^{-9}	14
$O(\alpha^5)$	-1.1×10^{-9}	-1.2×10^{-9}	-6.6×10^{-11}	1.8×10^{-10}	-1.2×10^{-10}	-5.3×10^{-11}	2.0×10^{-10}	15
$O(\alpha^6)$	-9.9×10^{-13}	-9.4×10^{-13}	5.3×10^{-14}	-1.6×10^{-12}	1.5×10^{-13}	9.3×10^{-14}	-1.7×10^{-12}	16
other	-3.0×10^{-12}	-3.2×10^{-12}	-1.8×10^{-13}	4.0×10^{-13}	-3.3×10^{-13}	-1.5×10^{-13}	4.5×10^{-13}	17
$d(\ln \mathcal{R}_{i,j})/d(\ln(m_p/m_e))$	0.33	0.38	0.041	-0.00067	0.088	0.047	0.0075	18
$d(\ln \mathcal{R}_{i,j})/d(\ln(m_d/m_e))$	0.17	0.19	0.021	-0.00034	0.044	0.023	0.0037	19

The unprimed ratios are dimensionless while the primed ratios $\mathcal{R}'_{m,n}$ are *dimensional* and weakly depend on R_∞. The omitted unit for column 5, rows 1 and 3, is Hz$^{0.13}$, and for column 8, rows 1 and 3, is Hz$^{0.14}$. In rows 6 - 8, the uncertainties due to the different fundamental constants are given individually, without considering correlations between the constants. The fractional uncertainties of the theoretical spin frequency values applied to the experimental frequencies are not included in row 2 but are listed in row 5, in the subsection of the theory values. In the total fractional uncertainty of the experiment - theory comparison (row 10), correlations between the uncertainties of the fundamental constants have been ignored, since they do not alter the result substantially. The lower half of the table (rows 11 - 19) presents the fractional contributions of various energy contributions to the theoretical ratios, as well as the normalized sensitivities on the mass ratios. The spin theory uncertainty is calculated assuming that the hyperfine theory uncertainties of the individual frequencies are not correlated, while for the QED theory uncertainty a correlation coefficient $r_{\mathrm{QED}} = 0.95$ is assumed. Taking into account the correlations of the hyperfine coefficients does not significantly change the experimental ratios and the total spin theory uncertainty.

Extended Data Table 5 | Least-squares adjustment LSA-3

Constant X	$X_{\text{LSA3}} - X_{\text{fiducial}}$	$u_{\text{r,LSA3}}$	$u_{\text{r,CODATA18}}$	$u_{\text{r,ab initio}}$
μ/m_{e}	$(-3.7 \pm 2.1) \times 10^{-8}$	1.7×10^{-11}	4.6×10^{-11}	–
R_{∞}	$(-0.63 \pm 2.1) \times 10^{-5}$ m^{-1}	1.9×10^{-12}	1.9×10^{-12}	–
r_{p}	(-0.0004 ± 0.0019) fm	0.0023	0.0023	–
$E_1(v=0,N=1)$	$(-6.8 \times 10^2 \pm 48.)$ Hz	1.5×10^{-6}	–	3.8×10^{-6}
$E_6(v=0,N=1)$	$(-1.6 \times 10^2 \pm 48.)$ Hz	5.5×10^{-6}	–	2.1×10^{-6}

LSA based on the three HD$^+$ transitions f_0, f_1, f_5. In this LSA the mass ratio is fitted while the constants R_∞ (row 3), μ/m_{e} (row 2), r_{p} (row 4) are adjusted. The CODATA 2018 values of R_∞ and r_{p} with their uncertainties are included as pseudo data. This mimicks a global fit that includes also atomic data. r_{d} is not separately adjusted but is assumed given by the squared difference of charge radii $\Delta r^2_{\text{pd}} = [r^2_{\text{d}} - r^2_{\text{p}}]_{\text{CODATA2018}}$, accurately known from hydrogen spectroscopy (Supplementary Information, Sec. A). The uncertainty of Δr^2_{pd} is neglected. Columns 2 and 3 are the results of LSA-3. The coefficients $\mathcal{E}_1$, $\mathcal{E}_6$ of level $v=0$, $N=1$ are included in the fit to reproduce four spin components of the rotational transition. Column 4 shows for comparison the current CODATA 2018 uncertainties. Column 5 is the uncertainty of a determination from a set of Penning trap measurements. One recognizes from a comparison of columns 3 and 4 that a reduction of the uncertainties of R_∞ and r_{p} compared to their CODATA 2018 uncertainties is not achieved, because the *ab initio* theory uncertainties of the HD$^+$ transition frequencies (and, to a lesser extent, their experimental uncertainties) are larger compared to the hydrogen atom case.